Remote Sensing of Environment 311 (2024) 114299

Contents lists available at ScienceDirect

Remote Sensing of Environment

journal homepage: www.elsevier.com/locate/rse

Heterogeneity in ice-wedge permafrost degradation revealed across spatial scales

Katherine N. Braun *, Christian G. Andresen

Department of Geography, University of Wisconsin-Madison, 550 N Park St, Madison, WI 53706, United States of America

ARTICLE INFO

Edited by Menghua Wang

Keywords:
Permafrost
Ice-wedge
Heterogeneity
Degradation
Mapping
Climate change

ABSTRACT

Permafrost thaw exhibits an array of spatially heterogenous patterns. As the Arctic continues to warm, those spatial patterns of permafrost thaw, or degradation, are becoming increasingly intricate and dynamic. In particular, ice-wedge permafrost degradation contains a high degree of spatial heterogeneity as ice wedges transition through undegraded, degraded, and stabilized stages. Developing accurate remote sensing methods for characterizing degradation will better allow us to monitor and forecast Arctic landscape evolution and associated land-atmosphere carbon-climate interactions. In this study, we (i) characterized ice-wedge degradation stages across a regional scale using a novel hydrogeomorphic approach. Then, we (ii) assessed the heterogeneity of degradation from meter- to kilometer-scales, and (iii) identified landscape properties associated with degradation patterns.

We leveraged the unique spectral and geometric properties of ice-wedge degradation stages to map those stages across 366 km^2 of the Arctic Coastal Plain near Prudhoe Bay, Alaska in sub-meter resolution Worldview-2 satellite imagery. Then, we validated the maps with in-situ observations, airborne LIDAR, and drone multispectral surveys. We evaluated spatial heterogeneity in ice-wedge degradation through a clustering approach. Specifically, we grouped regions into hydrogeomorphic clusters defined by similarities in trough widths and flooding, which reflect distinct degradation stages. This analysis revealed that ice-wedge degradation is heterogeneous across both meter and kilometer scales. At the meter scale, a single ice-wedge polygon is generally bounded by varied degradation stages. In addition, the most advanced stages of degradation occur in areas of low trough relative elevation and at the junctions between troughs. At the kilometer-scale, distinct clustering of degradation stages was identified across the region and linked to spatial patterns in topography: regional clusters of advanced degradation occurred in higher elevation areas. The millennial-scale evolution of the landscape has resulted in heterogeneous topographic, hydrologic, and cryogenic characteristics; these varied features exhibit diverse responses to warming events, which reflect the dynamic interplay that occurs between permafrost landscapes and climate change.

1. Introduction

Landscapes are often conceived of as intricate mosaics showcasing a rich array of patches scattered across the surface in spatially heterogeneous patterns (Pickett and Cadenasso, 1995). Spatial heterogeneity, the uneven variation in spatial patterns, is a description of complexity that is necessary to consider when examining landscape diversity, arrangement, and evolution. In the Arctic, permafrost and cryogenic processes produce complexly patterned landscapes; trends from meter-scale microtopography to regional geomorphology showcase that this complexity extends across spatial scales (Jorgenson et al., 2022; Lara et al., 2015; Nitzbon et al., 2021; Wainwright et al., 2021; Wolter et al., 2016). Permafrost degradation is reworking these Arctic landscapes and causing ecosystem changes (Andresen et al., 2020; Jorgenson et al., 2015; Marcot et al., 2015; Schuur et al., 2015; Vincent et al., 2017) with significant impacts on global climate feedbacks (e.g. Schuur et al., 2015). Understanding the spatial patterns and temporal dynamics of permafrost degradation, however, remains a significant challenge. Rather than occurring uniformly, degradation can manifest as an irregular and abrupt process where patterns vary across the landscape (Turetsky et al., 2020). The characterization of these complex processes is essential for improving our ability to forecast the evolution of the

* Corresponding author at: 550 N Park St, Madison, WI 53706, United States of America.
E-mail addresses: knbraun@wisc.edu (K.N. Braun), candresen@wisc.edu (C.G. Andresen).

https://doi.org/10.1016/j.rse.2024.114299
Received 31 October 2023; Received in revised form 5 June 2024; Accepted 24 June 2024
Available online 4 July 2024

Arctic landscape.

Polygonal tundra, formed by ice wedges and underlain by permafrost, is a prevalent landscape in the Arctic (Lachenbruch, 1962; Leffingwell, 1915). Ice wedges compose between 10 and 50% of massive ground ice in the Beaufort Sea region of Alaska (Kanevskiy et al., 2013), and the resulting ice-wedge landscapes cover 65% of the Arctic Coastal Plain of Alaska (Lara et al., 2018). Freeze-thaw cycles create soil cracks that infill with water in the spring and then freeze in the fall. Over decades and centuries, the infilling of these frost cracks forms ice wedges that can be meters in depth. Ice wedges underlie troughs and surround polygons that range from 10 to 30 m in diameter (Opel et al., 2018). Arctic soils are bound laterally by these ice wedges and vertically by frozen permafrost, thus the pressures generated by freeze-thaw cycles are directed upwards and buckle and thrust the land into distinctive polygonal patterns (French, 2017; Fig. 1).

Research on ice-wedge landscapes has historically focused on understanding the physical surface processes that form these landscapes (Black, 1982; Mackay, 1993; Plug and Werner, 2002), as well as theorizing on the relation of ice-wedge landscapes to drained thaw lake basins (Billings and Peterson, 1980; Hinkel et al., 2003). With the intensification of climate change over the past decade, landscape changes in the Arctic have accelerated. Consequently, research efforts have increasingly focused on unraveling the complex, multidirectional relationships between topography, vegetation, climate, and carbon dynamics as ice wedges undergo melting and stabilization (e.g., Koch et al., 2018; Liljedahl et al., 2016; Martin et al., 2018; Wolter et al., 2016). Intensive field studies have determined that the loss of ice wedges and associated impacts, termed degradation, is a quasi-cyclic process that can be organized into multiple stages of degradation and stabilization. The thawing of ice wedges occurs in distinct degradation stages where ice melts, the surface subsides, and water pools in deepening troughs. Eventually, however, the accumulation of organic matter and vegetation in troughs can sufficiently insulate the underlying ice wedge from further thaw, thus moving the ice wedge into a stabilized stage (Jorgenson et al., 2015, 2022; Kanevskiy et al., 2013, 2017). Mapping ice-wedge degradation stages (Fig. 2) provide a means for understanding the timing and extent of permafrost thaw and associated biogeochemical processes in ice-wedge landscapes.

The observed ice-wedge degradation across the pan-Arctic in recent decades has motivated the development of remote sensing techniques to map polygons and trough networks. Automated ice-wedge mapping projects have used machine learning techniques, such as convolutional neural networks, to automatically detect ice-wedge polygon boundaries in vast quantities of imagery (Abolt and Young, 2020; Bhuiyan et al., 2020; Witharana et al., 2020; Zhang et al., 2018). Such techniques have successfully delineated polygons and classified morphology (low-centered and high-centered polygons) in high-resolution imagery (Zhang et al., 2018). The trough areas, as opposed to polygon centers, have also been delineated using object based image analysis (Witharana et al., 2021). Another approach leveraged airborne LiDAR data to delineate trough networks, allowing for the examination of network evolution through time (Rettelbach et al., 2021). Methods for mapping ice-wedge degradation use open water in remotely sensed spaceborne and airborne imagery as a proxy for degradation (Fraser et al., 2018, 2022; Frost et al., 2018; Jorgenson et al., 2006; Steedman et al., 2017) or rely on manual classifications to identify degradation stages (Jorgenson et al., 2022; Wickland et al., 2020). We know of no work that has used remotely sensed data to quantitatively assess degradation stage, though such a method would be crucial for extending our detailed understandings of ice-wedge degradation and stabilization dynamics from field studies to regional and pan-Arctic scales.

Permafrost degradation is variable across scales. In particular, it has become evident through field observations on the Arctic Coastal Plain that an individual polygon can exhibit various degradation stages (Jorgenson et al., 2015; Kanevskiy et al., 2017). These stages include the highly visible flooding of the advanced degradation stage, but also more nuanced distinctions between undegraded ice wedges and degraded ice wedges that have progressed to stabilization. There is a noticeable gap in assessing regional heterogeneity in ice-wedge degradation: distinctions between geomorphic units such as drained thaw lake basins and interstitial tundra are clear (Lara et al., 2015, 2018), yet the variability within these individual units has not been well-quantified, leaving questions about where ice wedges are degrading and why. Exploring this spatial heterogeneity in permafrost degradation is crucial for unraveling the underlying drivers of permafrost thaw, pinpointing the locations most susceptible to degradation, and enhancing the accuracy of earth system models that aim to better represent the permafrost-climate feedback.

Examining variability in permafrost degradation requires quantifying spatial heterogeneity. Metrics for examining heterogeneity include assessments of spatial autocorrelation (how similar or dissimilar nearby objects are to each other; Anselin, 1995), rugosity (a measure of surface roughness; Loke and Chisholm, 2022), fractal dimension (a measure of the complexity of a fractal pattern; Loke and Chisholm, 2022), and variograms (a measure of variance between sample pairs in a spatial dataset; Garrigues et al., 2006). In ice-wedge landscapes, heterogeneity is present at multiple spatial scales, from within individual soil profiles (Siewert et al., 2021), to the polygon scale (Wainwright et al., 2015), to the regional scale (Nitzbon et al., 2021). Mesoscale landforms including lakes, drained lake basins, and the locations of interstitial tundra

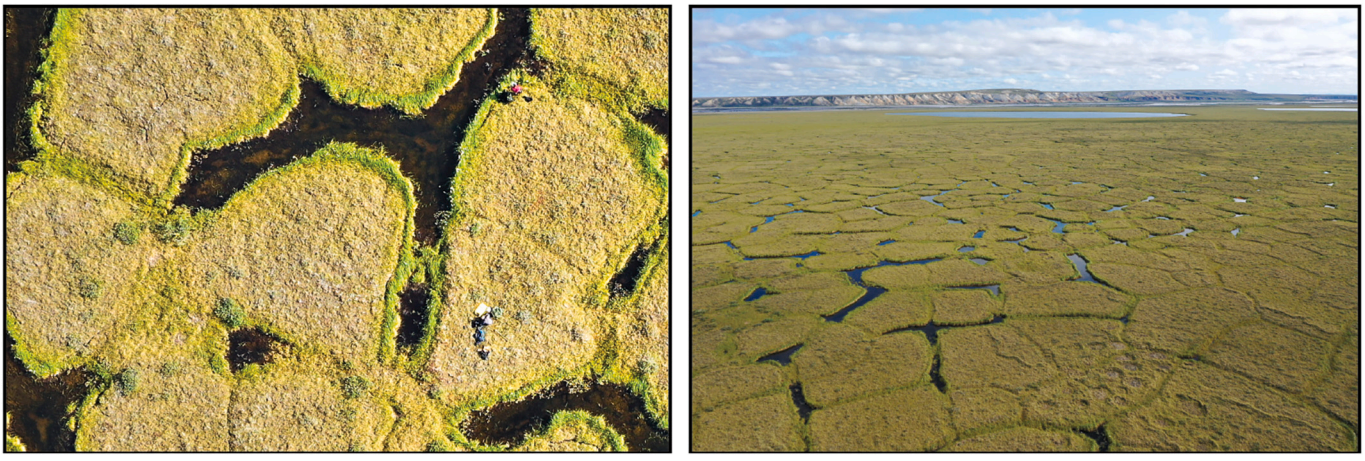

Fig. 1. Ice-wedge degradation produces heterogeneity in the patterns and dynamics of thermokarst across scales, from the polygon level (left, see people for scale) to the regional (right).

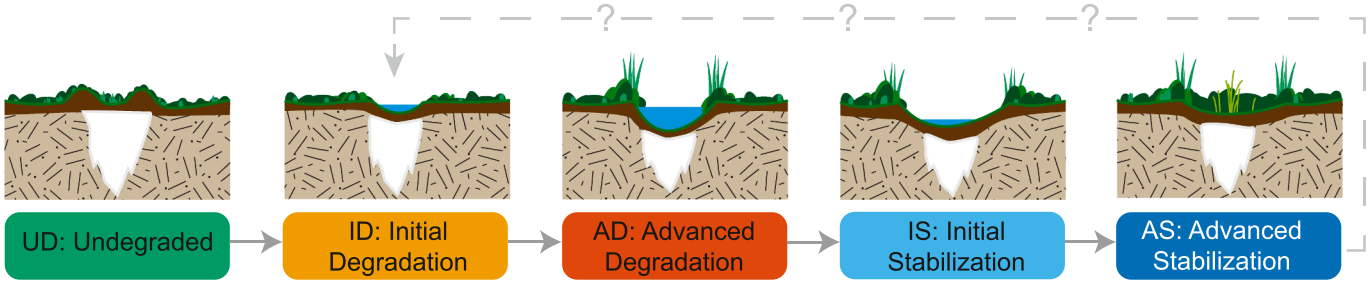

Fig. 2. The five-stage classification used in this work to differentiate ice-wedge troughs based on the progression of degradation and stabilization. The cross-sectional diagrams show changes in surface hydrology, soils, vegetation, and ice wedge state as degradation and stabilization progress. Green: undegraded; Orange: Initial Degradation; Red: Advanced Degradation; Light blue: Initial Stabilization; Dark blue: Advanced Stabilization. Diagrams not to scale. (For interpretation of the references to color in this figure legend, the reader is referred to the web version of this article.)

produce a patchwork of heterogeneity at the kilometer-scale (Lara et al., 2015; Nitzbon et al., 2021), though heterogeneity also exists within each of those landform types. Tundra microtopography associated with ice wedges is a main control on landscape characteristics such as vegetation, active layer thickness, soil moisture, and net ecosystem-exchange (Jorgenson et al., 2022; Wainwright et al., 2021; Wolter et al., 2016). Mapping and understanding this heterogeneity is crucial for predicting and managing the impacts of climate change in the Arctic. Therefore, in this paper, we (i) introduce a new approach employing multi-scale remote sensing for detecting and delineating stages of ice-wedge degradation troughs. Then, we (ii) examine spatial heterogeneity in degradation stage, and (iii) identify spatial landscape factors associated with permafrost degradation at both the meter and kilometer scales.

2. Methods

2.1. Study site

The study site is located in the Arctic Coastal Plain of Alaska along the Dalton Highway, ~50 km south of Prudhoe Bay, Alaska on the traditional lands of the Inupiat (Fig. 3). The Arctic Coastal Plain is a broad, level plain of low stature tundra that ranges in elevation from sea level at the Beaufort Sea and Chukchi Sea in the north to about 300 m above sea level at the foothills of the Brooks Mountain range in the south. The plain is dotted with numerous lakes, lake basins, and marshes. Vegetation is dominated by sedges, mosses, dwarf shrubs, and lichens (Raynolds et al., 2019). The Arctic Coastal Plain has an average temperature of −12 °C to −6 °C and can reach extreme lows of −51 °C in winter; precipitation is 180 mm/yr on average (Bailey, 1995).

The Arctic Coastal Plain is underlain by continuous permafrost. Soils

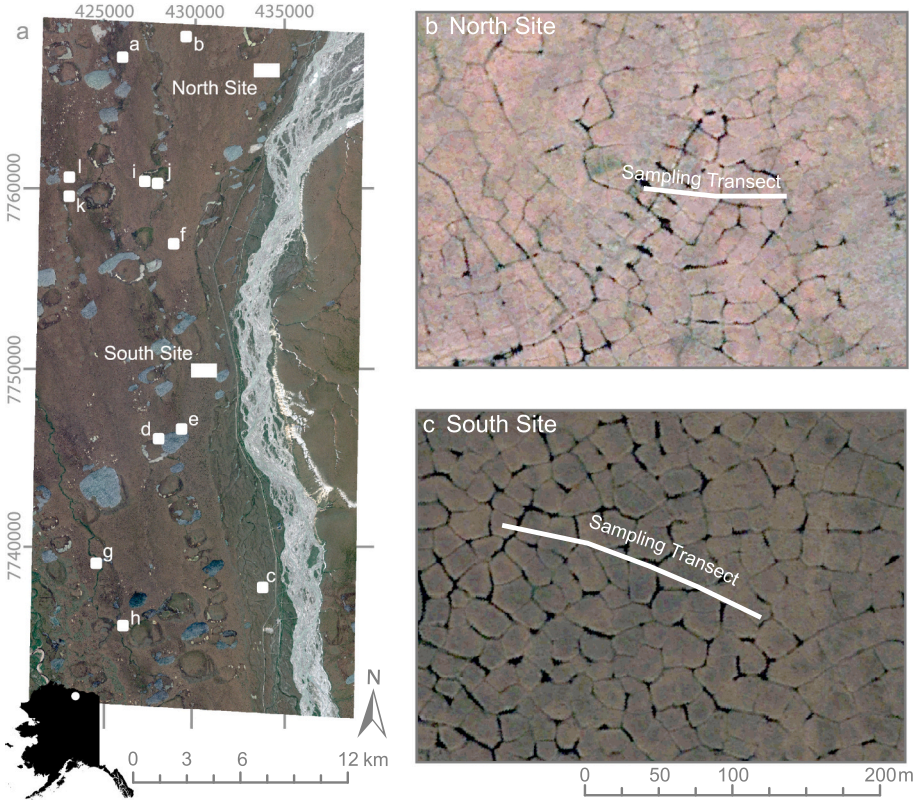

Fig. 3. Study site map. a: WorldView-2 satellite image of the study site in July 2014, with graticules indicating location in UTM Zone 6 North, meters (Imagery © 2014 Maxar). The two field sites are annotated with boxes, the 12 remote sensing focus sites are annotated with squares and alphabetical labels. Inset Alaska map shows location of study site on Arctic Coastal Plain; b: the North field site and 100 m sampling transect; c: the South field site and 250 m sampling transect.

are 98% Gelisols (Cryosol Working Group, 2014) and subsurface materials consist of unconsolidated marine and non-marine sand, silt, clay, and gravel of Quaternary age (Rawlinson, 1990). This material varies in thickness from a thin mantle to 50 m in depth and was deposited in the mid-Wisconsinian during the last major marine transgression. Parent material is also sourced from eroded material from the Brooks Range, which consists of calcareous bedrock (Parkinson, 1978), though the site examined in this work is located next to the Sagavanirktok River and likely is formed of fluvially transported parent materials. The surface of the Plain contains microrelief that is generally <1 m in height, though pingo landforms can reach heights of 15 m. In addition to vast extents of ice-wedge polygon networks, other landforms of note on the Plain include palsas, which are peat mounds with an ice core, as well as smaller-scale features including frost boils and ground stripes (Jones et al., 2008). Permafrost degradation has been observed extensively throughout the Arctic Coastal Plain, both at individual field sites (Jorgenson et al., 2015, 2022; Wickland et al., 2020) and also through repeated InSAR mapping which identified regional degradation-induced subsidence (Liu et al., 2010).

This study examined ice-wedge degradation at two scales: the meter scale (where characteristics vary between polygon centers, rims, and troughs) and the kilometer scale (where topographic variations and mesoscale landforms impact polygonal terrain location). Ice-wedge degradation at the meter scale was examined in July 2022 at two field sites, each ~1 km^2 in extent and located ~1.5 km west of the Dalton Highway (i.e., beyond the influence of road dust; Walker et al., 2022), as well as at 12 additional remote sensing focus sites, each 150 × 150 m in extent (Fig. 3). Ice-wedge degradation at the kilometer scale was examined via analysis of high-resolution commercial satellite imagery and airborne LiDAR data which covered a region approximately 38 by 14 km, containing 366 km^2 of ice-wedge terrain (Abolt and Young, 2020).

To examine spatial patterns in ice-wedge degradation, we used a combination of remote sensing data (drone surveys, airborne LiDAR, and satellite imagery) and field data. The sequence of datasets, methods, analyses, and resulting products are described below and illustrated in Fig. 4.

2.2. Field examination of ice-wedge degradation

In July 2022, we conducted field surveys to characterize ice-wedge degradation in situ. We present a suite of degradation stage classification methods (biophysical data analysis, drone imagery assessment, and drone spectral and topographic analysis) that we analyzed in concert to determine degradation stage (Fig. 2). Other more rigorous field assessments of ice-wedge degradation stage rely on soil and cryostratigraphic analysis (e.g., Jorgenson et al., 2015; Kanevskiy et al., 2017; Wickland et al., 2020), which was not possible for this study.

We collected biophysical data along transects to assess stages of degradation following methods outlined in previous work (Jorgenson et al., 2015; Kanevskiy et al., 2017; Wainwright et al., 2021; Wickland et al., 2020). In particular, biophysical data was collected every 10 m along the following transects: 100 m in length at the North site and 250 m at the South site. When an ice-wedge trough was within 5 m of the sampling point, the trough was measured (n = 24), otherwise the polygon was measured at the transect sampling point and attributed as polygon center (n = 9). Biophysical measurements include thaw depth, trough depth relative to the trough rim, water level of standing water,

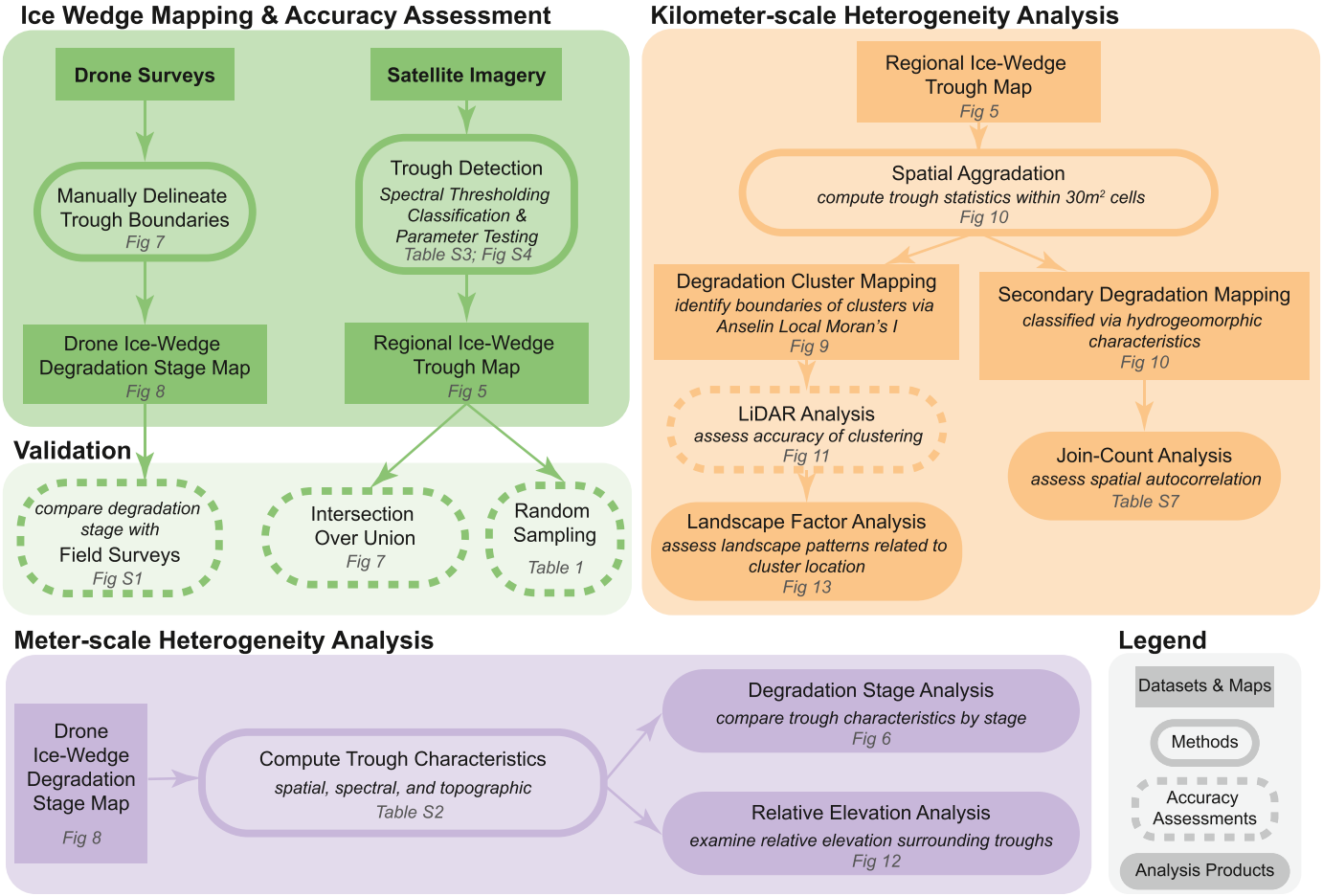

Fig. 4. Flow chart of datasets, processing methods, accuracy assessments, and analysis products produced in this work.

soil moisture, soil temperature, and vegetation cover and composition (to plant functional types; Macander et al., 2017). Each transect included samples of all stages of degradation present at each site; the initial stabilization and advanced stabilization stages were not found at either field site, which aligns with previous work indicating that this region experienced a major degradation event in the early 2000s and thus most ice-wedge troughs at this location have not had sufficient time to begin stabilizing (Liljedahl et al., 2016; Wickland et al., 2020). The two stabilization stages are therefore not included in further analysis. Statistical analysis of biophysical data included summary statistics, ANOVA, and Tukey's HSD test to compare groups. All statistical analysis was performed in R 2021.09.02 using tidyverse (Wickham et al., 2019), ggplot2 (Wickham, 2016), dplyr (Wickham et al., 2023), ggpubr (Kassambara, 2023), FSA (Ogle et al., 2023), lattice (Sarkar, 2008), patchwork (Pedersen, 2024), and agricolae (de Mendiburu and Yaseen, 2020) packages.

2.3. Drone data collection

A DJI Mavic 2 Pro with a 20 MB camera was flown using the UgCS PC mission planning software over the two sites to collect RGB imagery at 75 m above ground level (AGL). These images were processed into digital surface models (DSM) and orthomosaics using the Pix4D software; this processing method is based on the Structure-from-Motion photogrammetry method which uses the spatial position of multiple images to reconstruct a three-dimensional model of the site (Westoby et al., 2012). A MicaSense RedEdge MX multispectral camera was deployed on a DJI Matrice 600 and flown at 75 m AGL. Multispectral imagery was radiometrically calibrated using a Micasense Calibrated Reflectance Panel following manufacturer protocols. The five-band (B, G, R, red edge, NIR) imagery was then processed into an orthomosaic raster in Pix4D. Drone products were processed without ground control points; resulting products were co-registered to the satellite imagery using 15–20 control points per site. The resulting data products are expected to have low absolute accuracy, but local distortions at the scale of analysis (i.e., trough to polygon level) are expected to be smaller than features of interest (Kalacska et al., 2020). All data were collected in WGS84 UTM Zone 6 N; elevation is reported in meters relative to the WGS84 ellipsoid.

2.4. Drone-based mapping of ice-wedge degradation stages

The boundaries of all ice-wedge troughs at the two study sites were hand-digitized at 1:150 scale in ArcGIS Pro 2.5.0 using a combination of drone RGB orthomosaics (5 cm resolution) and relative elevation DSMs (5 cm resolution). The relative elevation DSM highlighted local breaks in topography and was used for delineating the boundaries of the troughs. The trough delineations included vegetation on the rims of troughs, therefore vibrant graminoids on the edges of flooded troughs were included within the trough based on field observations that these graminoids were rooted within the trough. Connected troughs that had visually distinct appearances were digitized into individual troughs so that each individual trough could be assigned an appropriate degradation stage: undegraded (UD), initial degradation (DI), or advanced degradation (AD; Table S2). This drone imagery assessment of stages was based on the visual appearance of the trough in the imagery and NDVI raster and previously published metrics of degradation (Table S1).

Spatial and topographic metrics were calculated for each individually delineated ice-wedge trough. Trough spatial metrics included area, length, average width, and perimeter. Trough length was generated with the Thin Raster tool in ArcGIS Pro to reduce the troughs into single-pixel wide linear features. Average trough width was assessed by calculating the total trough length per feature and then dividing trough area by length. Spectral statistics were only generated for the South site. Spectral metrics included Normalized Difference Vegetation Index (NDVI) and the NIR band (842 nm) values derived from the MicaSense camera; these metrics were chosen to examine differences in vegetation (NDVI) and surface water (NIR). The topographic metric examined was relative elevation, produced using a 5-m circular averaging filter. Spectral and topographic statistics were calculated for each trough feature using the Zonal Statistics as Table tool in ArcGIS Pro.

2.5. Satellite-based mapping of ice-wedge troughs

Three cloud-free, overlapping WorldView-2 image tiles from the Prudhoe Bay region (Fig. 3), taken on 7 July 2014, were used for the satellite mapping. The WorldView-2 panchromatic band (450–800 nm, 0.50 m resolution) was used to pansharpen the multispectral bands (blue: 450–510 nm, green: 510–580 nm, yellow: 585–625 nm, red: 630–690 nm, red edge: 705–745 nm, NIR1: 770–895 nm) from 2.1 m to 0.50 m resolution using the Gram-Schmidt method in ArcGIS Pro (Maurer, 2013). The three pansharpened images were mosaicked together and clipped to the extent of the site. Open water bodies, ice/snow, fluvial landforms, and developed land identified in the 2011 National Land Cover Database map (Homer et al., 2015) were masked from the image to focus on the ice-wedge landscapes of interest.

Satellite pixels corresponding to flooded ice-wedge troughs were extracted using a thresholding method on a Near Infrared (NIR1; 770–895 nm) difference raster. The NIR band was chosen to identify the flooded troughs in accordance with existing work on detecting flooded ice-wedge thermokarst pits (Frost et al., 2018). As flooded troughs only represent a portion of all ice-wedge troughs, pixels corresponding to dry troughs were extracted using a thresholding method on a modified NDVI difference raster as described below. Vegetation type is known to vary with polygon microtopography, especially along the margins of ice-wedge troughs (Wolter et al., 2016), thus leaving a visual signal in vegetation color that delineates the boundaries of ice-wedge troughs. We use this relationship between trough morphology and vegetation to identify dry troughs with NDVI.

We detected flooded and dry ice-wedge trough pixels through the following workflow: first, a difference raster was produced from the original single-band raster (NIR or NDVI for flooded and dry troughs, respectively) and from an averaged raster produced using a circular averaging filter (Fig. 5a-c). This difference raster highlights pixels that diverge from the local average. Iterative thresholding was conducted on the difference raster to identify the threshold that extracted the pixels of interest to the highest accuracy level (Fig. 5d-e). Finally, the resulting binary map of extracted pixels was cleaned using morphological opening to smooth jagged edges to more realistically mimic the natural boundaries of troughs (Haralick et al., 1987). Clusters consisting of fewer than 16 pixels (4 m^2) were deleted to reduce noise (Fig. 5f).

We optimized the processing workflow by conducting parameter testing, which identified the most effective averaging filter size, extraction threshold, and raster cleaning methods (see Supplemental Methods S1.2). Optimal parameters were identified for each stage of the processing workflow by comparing the resulting maps' accuracy assessment, determined from 500 equalized stratified random ground truth samples. The optimization assessment was conducted on a subset of the regional site with ground truth samples independent of the regional site accuracy assessment ground truth data. The resulting dry trough and flooded trough classified maps were combined into a final three-class map depicting non-trough areas, dry troughs, and flooded troughs.

Two methods were used to assess the accuracy of the final ice-wedge trough satellite map. First, we conducted a standard accuracy assessment across the full satellite map footprint using 425 equalized stratified random samples, where ground truth was identified visually in the true color satellite image. Second, within the two field site footprints, the trough pixels identified in the satellite map were compared to the boundaries of troughs hand-digitized from the drone data in order to examine biases in the satellite-based map based on degradation stage. The two maps were compared using the intersection-over-union (IoU)

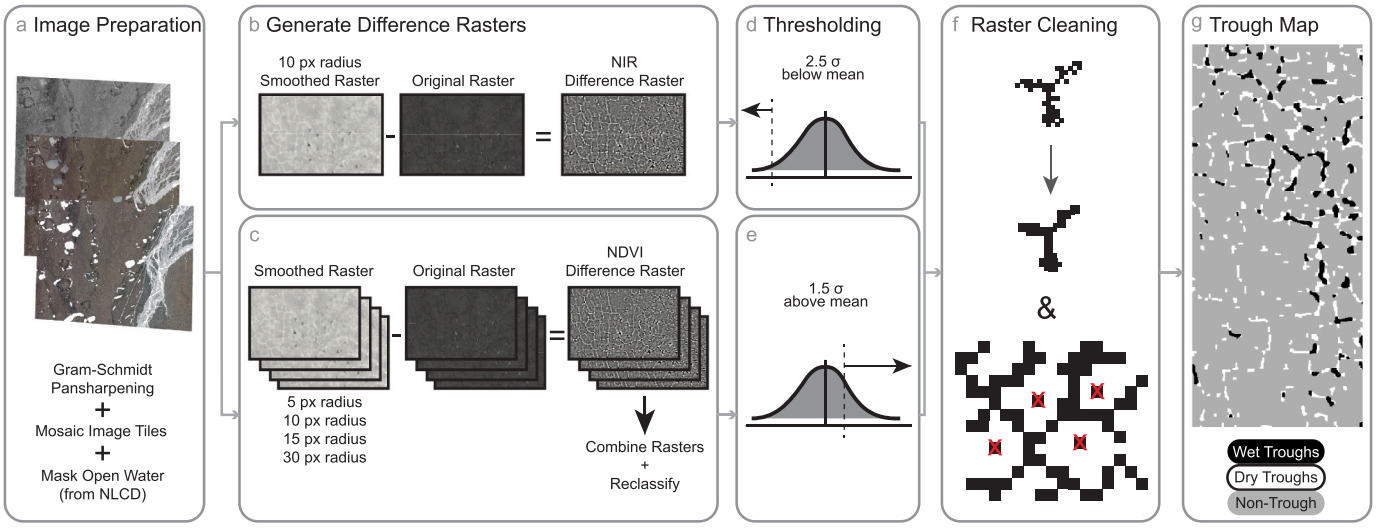

Fig. 5. Ice-wedge trough mapping workflow: first (a), Satellite WorldView-2 images were prepared for the classification process through pan-sharpening the lower-resolution multispectral imagery to the panchromatic band (Imagery © 2014 Maxar). Three images covering the study site were mosaicked together, and then non-polygonal tundra areas were masked from the image using the NLCD 2011 map. Then, difference rasters were generated to highlight portions of the landscape with strong contrasts in surface water, detected with the NIR band (b), and vegetation, detected with NDVI (c), which correspond to flooded troughs and dry troughs, respectively. The NIR difference raster was produced once, using a 10 px radius averaging window. The NDVI difference raster was produced four times, with differing average windows, then those four rasters were combined and reclassified into a final dry trough map. The pixels belonging to troughs were extracted from the difference raster using thresholding (d, e), and the resulting trough maps were cleaned (f) to produce the final, three-class trough map (g).

method to examine how much trough area the satellite method accurately detected, using the drone-based delineations as ground truth (Chen et al., 2021; Hsu et al., 2020; Rezatofighi et al., 2019). It is important to note that between 2014 and 2022, no significant degradation events are documented. Minor degradation events typically result in trough boundary shifts of centimeters to decimeters, falling below the 0.5 m resolution of WorldView imagery. Thus, no notable transitions in degradation stage (e.g., from initial to advanced degradation) were expected to occur. Thus, we are confident that comparing the 2014 and 2022 trough maps does not significantly impact the ground truthing.

2.6. Regional classification, clustering, and drivers of degradation stage

2.6.1. Spatial aggregation of ice-wedge trough characteristics

We employed a spatial aggregation approach to examine large-scale patterns in trough surface hydrology, geomorphology, and distribution. This aggregation is necessary in order to derive regular spatial statistics on irregular trough features; producing these aggregated spatial statistics allows for quantitative classification of degradation stages. Zonal statistics within a 30- square grid were conducted over the full satellite site footprint (366 km^2 of ice-wedge terrain); the 30-m grid was chosen to align with the typical width of a polygon. Zonal statistics within each cell of the grid were calculated in ArcGIS Pro: total non-trough area, dry-trough area, and flooded-trough area. Total trough length per cell was generated via skeletonization (Rettelbach et al., 2021): the dry and flooded trough classes were reclassified into a single class, then the Thin Raster tool in ArcGIS Pro was used to reduce the multi-pixel trough features into single-pixel wide linear features. Average trough width was determined per cell by dividing the total trough area by the trough length. The percentage of flooded pixels per total trough area was also calculated per cell.

2.6.2. Spatial clusters in degradation stage

To quantify the regional spatial heterogeneity in ice-wedge degradation, we used a spatial clustering method, Anselin Local Moran's I, to identify the locations of degradation clusters. Anselin Local Moran's I (run within ArcGIS Pro's Cluster and Outlier Analysis tool) identifies hot spots and cold spots in quantitative data by comparing each value to its neighborhood (Anselin, 1995).

We used Anselin Local Moran's I on two inputs: the aggregated grid of average trough width, and the aggregated grid of trough flooding. The two resulting cluster maps, depicting hot spots and cold spots in trough width (geomorphology) and trough flooding (hydrology), were combined via overlay to produce a map depicting four classes of statistically different trough hydrogeomorphology. Clusters with low average trough width are hypothesized to occur in locations with troughs dominantly in the initial degradation and advanced degradation stages. Within those areas, high flooding clusters are assumed to have dominantly advanced degradation troughs, given that flooded troughs and thermokarst pits are characteristic of this stage (Kanevskiy et al., 2017; Wickland et al., 2020). Clusters with high average trough width are hypothesized to have dominantly either initial stabilization or advanced stabilization troughs, where the distinction between initial and advanced stabilization is determined by the amount of flooding present (i.e., high flooding = initial stabilization, low flooding = advanced stabilization; Kanevskiy et al., 2017; Wickland et al., 2020).

The hydrogeomorphology clustering method identified areas with distinct variations in trough surface hydrology and geomorphology; whether these variations correspond to the dominant degradation stage within each cluster required further examination. We conducted further remote sensing analysis at 12 focus sites to determine what finer-resolution patterns in ice-wedge degradation the clusters were identifying throughout the region. These focus sites examined the full spatial range of the regional site, beyond the locations that were physically accessible for field sampling. We used an airborne LiDAR dataset collected in 2012 and 2014 (e.g. coterminous with the WorldView site bounds and acquisition date) with ground point density of >20 pts./m^2 (Abolt and Young, 2020) for topographic analysis at the focus sites.

Within each of the four hydrogeomorphology classes, three 150 × 150 m sites were randomly selected for analysis. The LiDAR point cloud was processed into 0.25 m resolution DEMs for each site and a macrotopography raster was produced as well, using a circular averaging filter of 20 m. For each site, the trough boundaries were manually digitized using the LiDAR DEM and macrotopography raster, aided by the WorldView imagery. Degradation stage was visually assessed for each trough. The accuracy of the satellite trough mapping method was

determined with the Intersection over Union (IoU) method.

2.6.3. Examining topographic drivers of degradation clustering

We analyzed how degradation stages differed in terms of topographic metrics produced at two scales. At the local scale, we examined how relative elevation, produced from the drone DSM, varied between degradation stages. We examined average relative elevation in the polygon areas immediately surrounding the ice-wedge troughs to determine whether degradation stage correlated with polygonal relative elevation (see Supplemental Methods S1.1).

Regional topographic metrics were generated using the 2 m ArcticDEM produced by the University of Minnesota Polar Geospatial Center (Porter et al., 2022). These metrics included average elevation and topographic position index (calculated with 500 m radius). Topographic position index describes the relative elevation of a point compared to its surroundings within a set radius (Weiss, 2001).

2.6.4. A secondary, independent assessment of degradation and heterogeneity

In addition to identifying the spatial clusters in ice-wedge hydrogeomorphology, we also assigned each 30-m cell of the 366 km^2 of ice-wedge terrain a dominant degradation stage based on the cell's average trough width and flooding percentage. Cells with average trough width below 1 m were assigned the undegraded stage, which aligns with field observations of ice-wedge troughs and other manual classifications of ice wedge stage in remotely sensed imagery (Wickland et al., 2020). The amount of surface water present was used to distinguish between initial degradation and advanced degradation. The advanced degradation classification was given to cells with over the mean amount of trough flooding: 6%; cells below this threshold were assigned the initial degradation stage.

These hydrogeomorphology-based classifications are proposed to correspond with the dominant ice-wedge degradation stage present within each cell. Cells with low average trough width (<1 m) are likely dominated by undegraded stages; cells with low flooding are likely dominated by initial degradation stages; cells with high flooding are likely dominated by advanced degradation stages. Stabilization stages were not assigned for this site, given the recent initiation of degradation and lack of stabilization observed in the field, however, stabilized stages could also be identified using this thresholding method by assigning a trough width threshold to distinguish between narrower, degraded troughs and wider, stabilized troughs.

The resulting regional degradation stage map contained visible clustering in stages across the region, similar in location to the Local Moran's I output. The join-count statistic with the queen's case was used to quantitatively assess whether the spatial patterns in degradation stage were statistically discernible. The join-count statistic is an assessment of spatial autocorrelation and determines whether a binary phenomenon is clustered, dispersed, or randomly distributed across a region (Feuillet et al., 2020; Henn et al., 2016; Murakami et al., 2005; Oyana, 2020). As the binary input for the join-count statistic represents presence and absence of a phenomenon, we conducted the join-count statistics three times, once for each degradation stage.

3. Results

3.1. Mapping and assessing ice-wedge degradation stages

All three methods of examining ice-wedge degradation stage at the field sites (drone imagery assessment, biophysical data analysis, drone spectral and topographic analysis) broadly agreed in degradation stage assessment. The biophysical data analysis (Fig. S1 and S2) and drone data analysis (Fig. 6) both confirmed that biophysical, spectral, spatial, and topographic characteristics vary between degradation stages. We

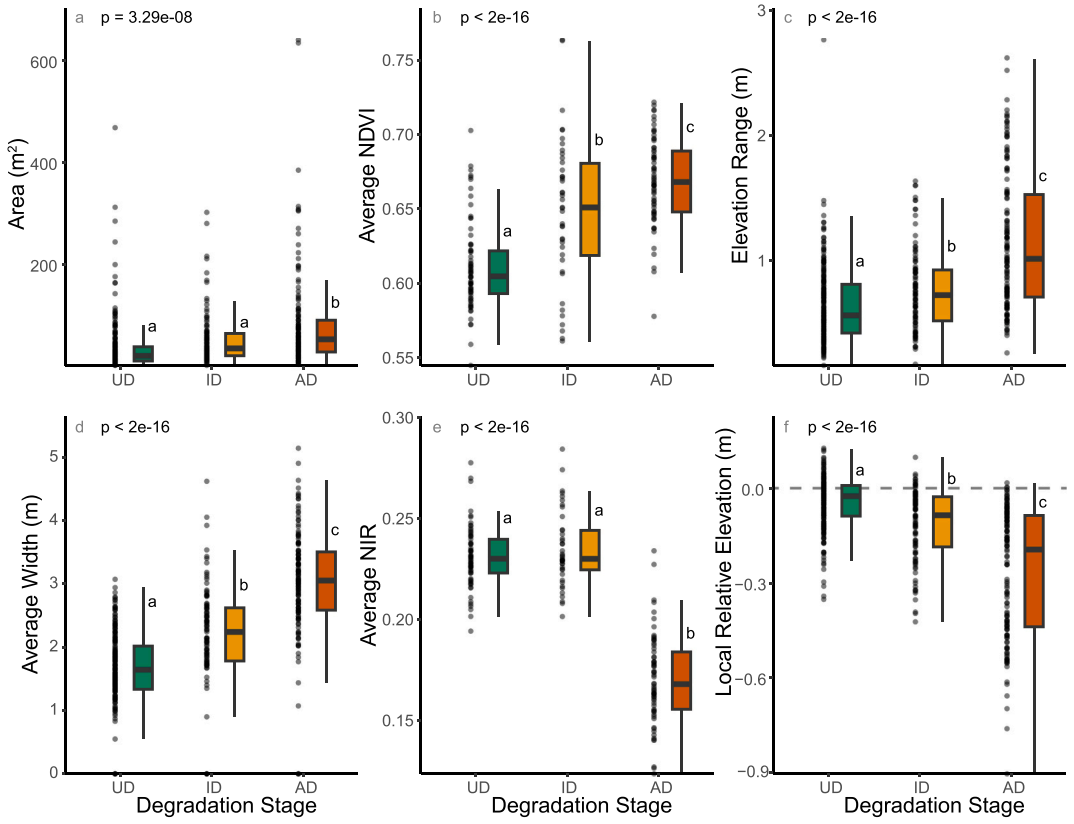

Fig. 6. Spatial (a, d), spectral (b, e), and topographic (c, f) characteristics of ice-wedge troughs as measured in the drone multispectral imagery and elevation data. UD: undegraded, DI: initial degradation, AD: advanced degradation. $n = 448$ for the spatial and topographic box plots (a, c, d, f); $n = 175$ for the spectral box plots (b, e). *P*-values indicate results of ANOVA test. Means that do not share any letter are discernibly different by the Tukey Test at the 5% level of significance.

consider the alignment in stage classification between independent methods sufficient evidence to accurately classify degradation stage.

Each in-situ biophysical variable was compared across degradation stages and highlighted major differences between stages (Fig. S1). Soil temperature, trough depth, water depth, and active layer depth had discernibly different values between degradation stages for the 24 troughs sampled in the field. Patterns in biophysical characteristics between degradation stages aligned with expectations; biophysical indicators of degradation such as trough width, depth, active layer thickness, and soil temperature all were greater in the advanced degradation stage troughs compared to the undegraded troughs (Table S1, Supplemental Text S2.1).

Each degradation stage had discernibly different spectral, spatial, and topographic characteristics based on the cm-scale drone imagery delineations. Trough area and average width both increased with degradation (Fig. 6). Average NDVI within each trough increased with degradation stage. The digitization of the trough boundaries included the trough rims which in many advanced degradation troughs contained bright green graminoids on the edges of the trough ponds, thus increasing the advanced degradation troughs' overall NDVI value despite the fact that these troughs were typically flooded. Average NIR within the undegraded and initial degradation troughs was significantly higher than the advanced degradation troughs, which typically were highly flooded. Elevation range increased with degradation, as undegraded troughs had the least difference in elevation between the edges and trough center (0.64 m), while advanced degradation troughs typically had elevation ranges >1 m (1.14 m). Local relative elevation was closest to 0 m at the undegraded troughs (−0.04 m) and had the highest magnitude (−0.27 m) in the advanced degradation troughs; advanced degradation troughs occurred in the lowest elevation portions of the trough network.

3.2. Satellite ice-wedge trough mapping

3.2.1. Optimizing satellite trough detection

Three parameters used in the satellite trough mapping method – the averaging filter size, extraction threshold, and noise removal – were tested to determine the highest accuracy method for trough identification. The averaging filter size and extraction threshold were tested with both NDVI and NIR layers to find the highest-accuracy parameters for identifying dry and flooded troughs respectively. The best NIR averaging filter size was a circular filter with a 10 pixel radius. The best NDVI averaging filter was a combination of all four filtering sizes (5, 10, 15, and 30 pixel radius). This method generated the most visually continuous troughs and was therefore chosen despite the fact that it was 1.4% lower in accuracy compared to the highest accuracy method (Table S5; Fig. S4). The highest accuracy extraction threshold for the NIR raster was 2.5 standard deviations below the mean; the highest accuracy extraction threshold for the NDVI raster was 1.5 standard deviations above the mean.

3.2.2. Satellite trough detection accuracy

Over the satellite-based regional map, non-trough area accounted for 90.2% of the site (330 km^2), dry troughs accounted for 8.7% of the site (32 km^2), and flooded troughs accounted for 1.1% of the site (3.9 km^2).

The different accuracy methods produced overall ice-wedge mapping accuracies ranging from 55 to 85%, depending on sampling approach and type of accuracy. The 425 equalized stratified random samples produced an overall accuracy of 55.4%. The sensitivity and specificity of the ice-wedge trough map by class was higher for the flooded trough class (87% and 83%, respectively), indicating that this method performed well at identifying the flooded troughs and was less proficient at identifying the non-flooded troughs (53% and 70%; Table 1).

The second accuracy assessment was an intersection over union comparison (IoU) between the satellite ice-wedge trough map and the manually digitized trough map based on the drone data. This comparison allowed us to examine how well the satellite map identified ice-wedge troughs by degradation stage, so we can understand the biases present in satellite-based data. The satellite method's overall pixel accuracy at distinguishing troughs and non-trough areas was 83% and 85% at the North and South sites respectively (Fig. 7). The satellite method performed best at identifying troughs in the advanced degradation stage (59% and 62% of AD trough area detected at the North and South site respectively), and the true positive rate decreased for the initial degradation stage (35% and 23%) and was poorest for the undegraded stage (19% and 8%). Examining the accuracy by degradation stage indicated that the satellite method was accurately identifying non-trough area, which covered the majority of the site, thus leading to the high overall accuracy. The method was less accurate at identifying degradation stages which only represented 20% of the site, leading to lower true positive rates for the troughs than non-trough areas.

Table 1
Regional accuracy assessment for the satellite trough detection method with 425 random equalized stratified points. Overall accuracy: 55.4%. Kappa: 0.3301.

	Non Trough (%)	Dry Trough (%)	Flooded Trough (%)
Sensitivity	45.1	53.1	87.2
Specificity	86.1	69.6	82.6
Balanced Accuracy	65.6	61.4	84.9

3.3. Spatial analysis of ice-wedge trough maps

3.3.1. Local patterns in degradation stage

At both field sites, ice-wedge troughs composed 20% of the total site area. In particular, troughs in the advanced degradation stage dominated at both sites; advanced degradation troughs comprised 47% of the total trough area, while undegraded troughs represented 31% and initial degradation troughs made up 22% of total trough area (Table S2). Advanced degradation troughs predominantly occurred at the intersections between multiple troughs, as determined by counting the proportion of advanced degradation troughs that contained an intersection (95%, $n = 137$; Fig. 8). The South Site had a relatively regular repeating pattern of ice-wedge troughs, whereas the North Site was impacted by the presence of a relict drainage pathway that appeared to have influenced ice-wedge formation and degradation (Fig. 8b). Frost boils at the North Site also interacted with some of ice-wedge troughs (Fig. S3).

3.3.2. Spatial clustering of trough hydrogeomorphology

Results from the Anselin Local Moran's I statistic identified hot-spot and cold-spot clusters in quantitative data. One-fifth of the regional site was identified as belonging to one of the four clusters, while the remaining four-fifths of the site did not exhibit clustering in ice-wedge hydrogeomorphology (Fig. 9). The two field sites (North Site and South Site) both fall within areas delineated as advanced degradation clusters where narrow, flooded hydrogeomorphology dominates. Both sites have a majority of digitized trough area (47%) in the advanced degradation stage (Table S2).

The secondary method of examining kilometer-scale ice-wedge degradation patterns used the thresholding technique to assign each 30-m cell a degradation stage (Fig. 10). This mapping identified 9% of the site as undegraded, 61% as initial degradation, and 30% as advanced degradation. The thresholding method provided another line of evidence indicating that trough properties vary significantly across the site, and that ice-wedge hydrogeomorphology, as a proxy for degradation stage, was heterogeneous across kilometer scales. The join-count statistic showed that all three hydrogeomorphology-based classes had statistically significant positive spatial autocorrelation ($p = 0.001$; Supplemental Table S7). Positive spatial autocorrelation indicated that nearby objects were more closely related to each other than further

Fig. 7. Comparing drone-based and satellite-based methods of delineating ice-wedge troughs. (a) Drone orthomosaic image of South Site. (b) Hand-digitized trough boundaries in black on drone orthomosaic base map. (c) Satellite-derived trough map. Dry ice wedge troughs in white, flooded troughs in black, and non-trough area in gray.

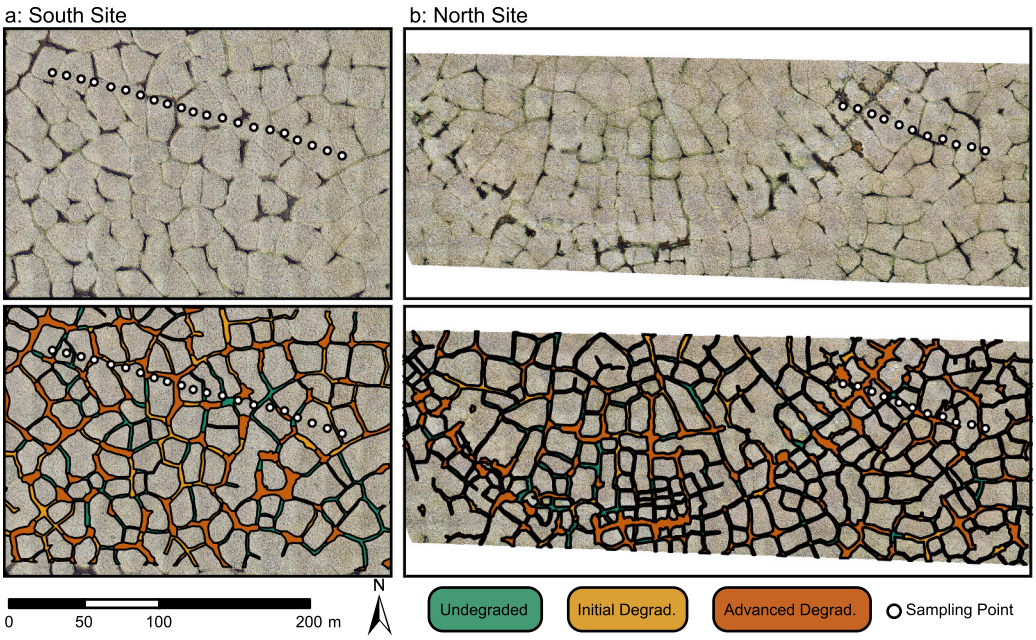

Fig. 8. Top: drone orthomosaics of the two study sites (a: South Site, b: North Site), with locations of transect sampling shown as white circles. Bottom: digitized trough boundaries, with color indicating qualitatively-assessed degradation stage.

objects; hydrogeomorphology classes were strongly spatially clustered at the kilometer scale. The thresholding method automatically assigned every cell of the input data a degradation stage, while the clustering method identified the portions of the landscape that contained statistically discernible spatial trends. As our objective was to understand the regional patterns in ice-wedge heterogeneity, the remaining analysis focused on the results of the clustering method which highlighted those regional clusters in degradation.

The 0.25 m resolution LiDAR analysis of twelve 150 × 150 m focus sites examined variability in trough characteristics and the ice-wedge mapping accuracy within the hydrogeomorphology clusters (Fig. 11). The manual delineation of ice-wedge troughs in the LiDAR data and assessment of trough stage from the satellite imagery showed that sites within the proposed advanced degradation cluster had the highest mean IoU (mIoU), indicating that the satellite-based ice-wedge mapping produced the best results in locations with large amounts of degradation. The satellite-based ice-wedge map had the lowest mIoU in the proposed advanced stabilization cluster, while the proposed initial degradation and initial stabilization clusters also had low mIoU values (Fig. 11). Examining the imagery for the sites showed that the proposed advanced degradation cluster was accurately identifying portions of the landscape where the majority of ice-wedge troughs were in either the advanced degradation or initial degradation stage. The other three hydrogeomorphology clusters were instead identifying locations with systematic biases in the satellite ice-wedge trough map. Two of those six sites in the initial and advanced stabilization clusters did not have any visible ice-wedge troughs in the LIDAR data nor imagery data (Fig. 11). Given both the known lack of wide-scale stabilization present at this site and the low accuracy of the cluster mapping in areas without advanced degradation, the remaining analyses focused exclusively on the advanced degradation cluster.

3.3.3. *Topographic patterns of degradation stage*

At the meter scale, the average relative elevation bordering each trough at the two field sites revealed that advanced degradation troughs were more likely to be lower on the local landscape (i.e., deeper; Fig. 12).

At the kilometer scale, hydrogeomorphology clusters occurred in distinct topographic regions (Fig. 13). The advanced degradation cluster occurred on the highest portion of the landscape, both in terms of average elevation and topographic position index. The remainder of the site had a lower average elevation (71.9 masl vs. 79.0 masl) and lower average topographic position index (0.06 m vs. 0.39 m). Note that the initial degradation, initial stabilization, and advanced stabilization clusters were included in the non-clustered category for this analysis (Fig. 13).

4. Discussion

4.1. *Ice-wedge degradation is heterogeneous across scales*

The multi-scale analysis of ice-wedge landscapes in this work

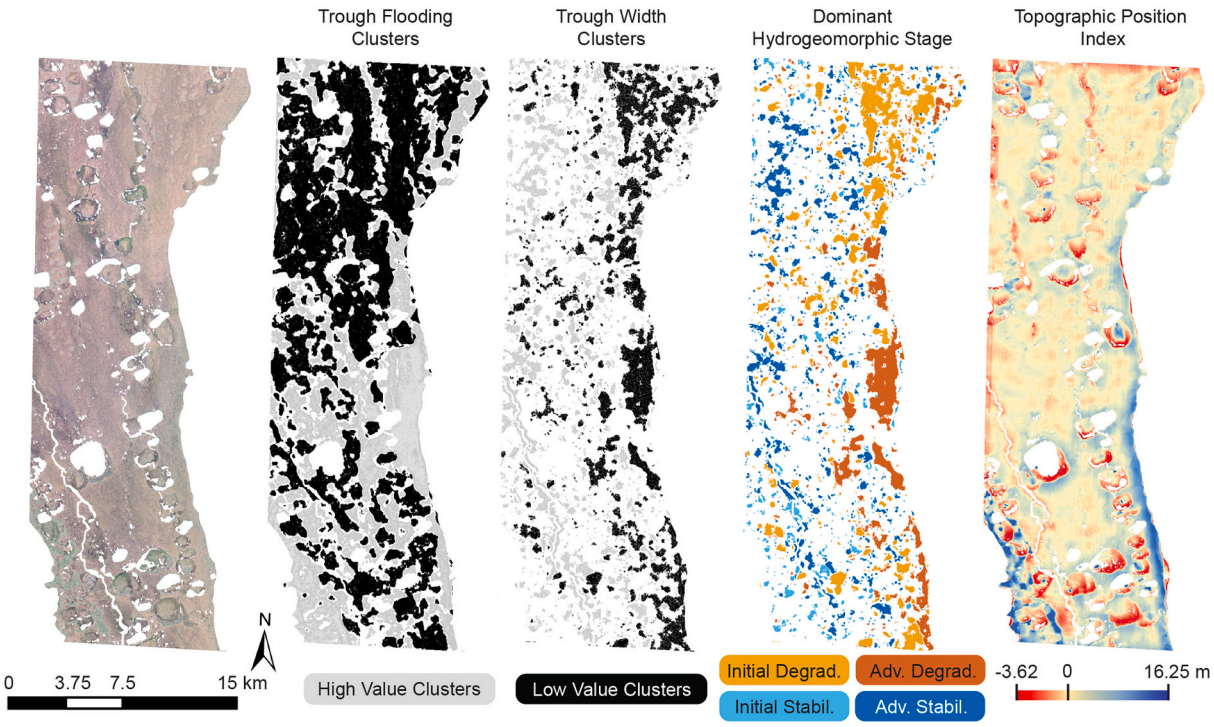

Fig. 9. Maps of the regional site depicting, from left to right, the WorldView-22,014 true-color imagery (© 2014 Maxar), the trough flooding cluster map, the average trough width cluster map, the hydrogeomorphology cluster map, and a raster of topographic position index, generated with a 500 m circular radius averaging filter on the ArcticDEM (courtesy of the Polar Geospatial Center).

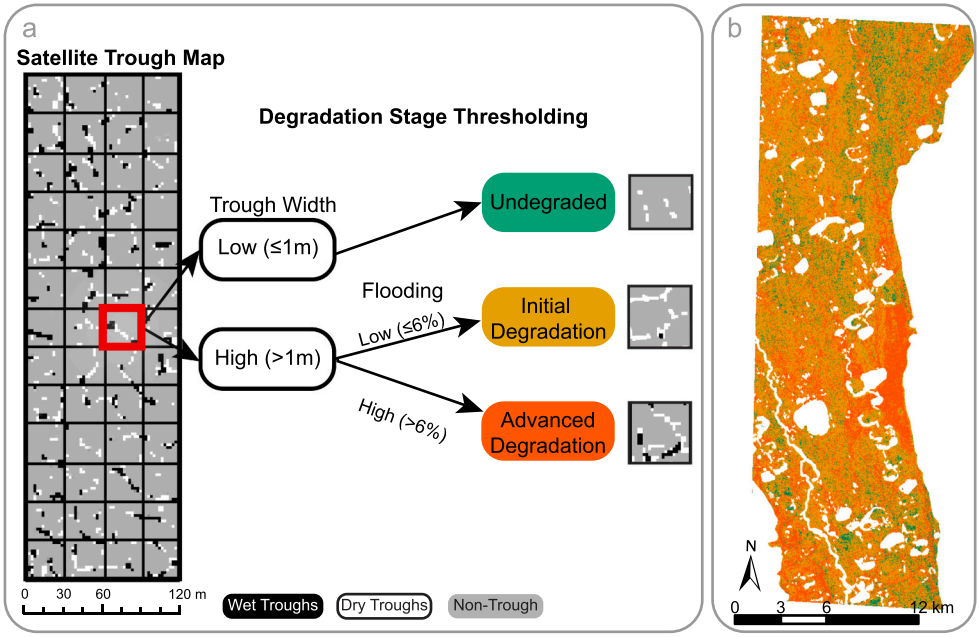

Fig. 10. Hydrogeomorphology-based classification method used to define dominant degradation stage within 30 m grid cells overlain on the satellite trough map. a: A two-stage classification scheme was used to distinguish each cell's hydrogeomorphic class based on the average trough width and percentage of flooding. The classification method used in this work featured three classes: undegraded, initial degradation, and advanced degradation. The hydrogeomorphic classes are assumed to correspond to the dominant degradation stage present within each cell and are labeled correspondingly; b: the degradation stage map across the full regional site. Colors in map b correspond to the degradation stages presented in panel a.

indicates that degradation is heterogeneous at both the meter-scale and kilometer-scale. Examining the spatial patterns of this disturbance regime is essential for assessing the underlying processes impacting the rate and magnitude of thermokarst formation, which is essential for improving our understanding of where and why permafrost undergoes thaw.

At the meter scale, stages of degradation have unique microtopographic signatures. The drone topographic analysis revealed that troughs in the advanced degradation stage occupy both the lowest relative elevation within the trough network (Fig. 6) and occur adjacent

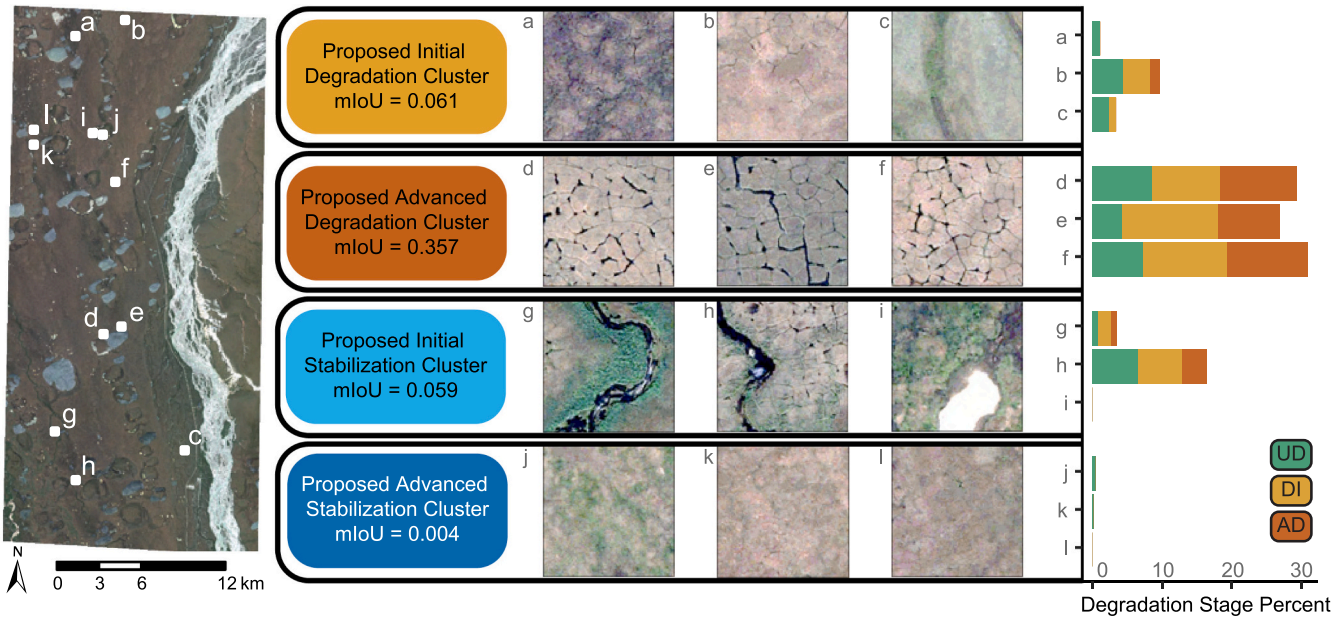

Fig. 11. Results of LiDAR analysis at 12 randomly selected focus sites. Left: WorldView-2 image of the regional site (© 2023 Maxar), with labeled locations of the 12 focus sites. Middle: images of each focus site, categorized by hydrogeomorphology cluster. Cluster label includes the mean Intersection-over-Union accuracy results for the three focus sites from that cluster; IoU is determined by comparing the hand-digitized "ground truth" delineation of ice-wedge troughs to the satellite-based trough map. Right: stacked bar plots indicating the percentage of each focus site that was manually classified into degradation stages.

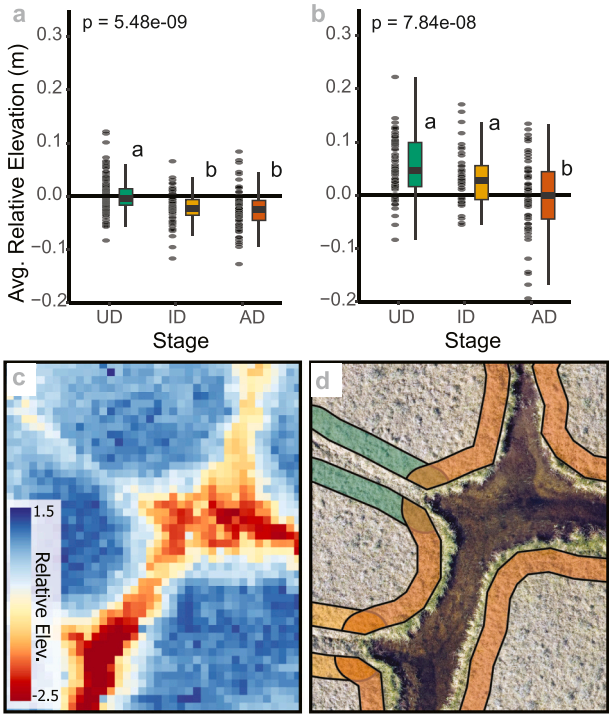

Fig. 12. Box plots depict the average relative elevation within a 1.5 m buffer in the ice-wedge polygon surrounding each trough. Black dots represent raw data. P-values indicate results of ANOVA test. Means that do not share any letter are significantly different by the Tukey-test at the 5% level of significance. a: Box plot for North site b: Box plots for South Site. c: Relative elevation raster from the South Site. d: Drone image with the relative elevation buffer overlain. Colors correspond to degradation stages (green: undegraded; yellow: initial degradation; red: advanced degradation). (For interpretation of the references to color in this figure legend, the reader is referred to the web version of this article.)

to the lowest elevation portions of the polygon center (Fig. 12). This finding aligns with a possible transition in polygon morphology as a response to warming, where flat-centered polygons experience degradation-induced subsidence at the polygon rim (i.e., along the ice-wedge troughs), transforming flat-centered polygons into high-centered polygons (Liljedahl et al., 2016). It is unknown if advance degradation occurring adjacent to the lowest portion of the polygon is a cause or consequence of degradation (or both). For example, the topographic low may have been present during the pre-degradation period, promoting the pooling of water, induced thermoerosion, and thus concentrated degradation as shown by modeling (Abolt et al., 2020; Nitzbon et al., 2021) and observational studies (Connon et al., 2018; Necsoiu et al., 2013). Alternatively, the topographic low may represent a post-degradation surface, where the low relative elevation surrounding advanced degradation troughs was produced by subsidence after degradation.

In addition to topography, we identified a consistent pattern of meter-scale degradation associated with ice-wedge geometry and geomorphic history. For example, 95% of troughs in the advanced degradation stage at the field sites are located at junctions where multiple ice-wedge troughs intersect (Fig. 7). These junctions have larger ice-wedge surface area and occur on the lowest relative elevation of polygons, leading to water pooling and degradation vulnerability (Fig. 12; Abolt et al., 2018, 2020; Nitzbon et al., 2021). Other factors such as geomorphic history may play a role in localized degradation. For example, a relict drainage pathway at the North site was observed to contain higher amounts of ice-wedge troughs and degradation (Fig. 8, Fig. S3). Subsurface characteristics can influence ice-wedges formation (Forte et al., 2022), and may consequently influence the spatial patterns of degradation observed at this site.

At the kilometer scale, this study shows that degradation, which is understood to occur nonlinearly at individual ice-wedges (Kanevskiy et al., 2017), also occurs in heterogeneous patterns at the kilometer-scale. While previous work has examined where ice-wedge polygons are most likely to occur (Steedman et al., 2017), little has been done thus far to assess regional trends within ice-wedge landscapes. Ice-wedge troughs are arranged in clusters of degradation (Fig. 9), suggesting the presence of underlying factors influencing regional variability in

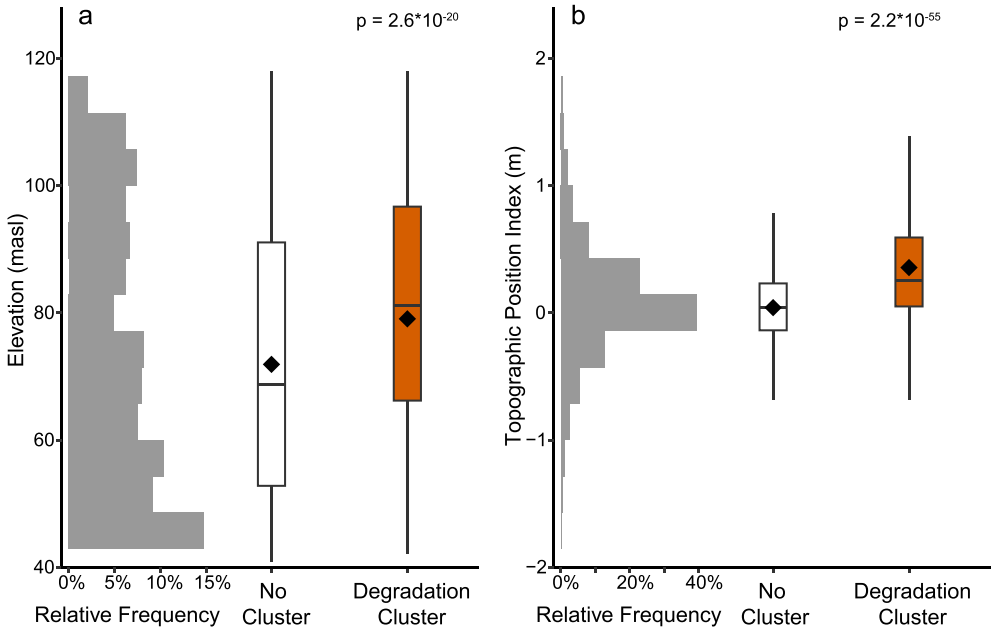

Fig. 13. Normalized relative frequency distributions and box plots depicting the data distribution for mean elevation (a) and topographic position index (b) as well as the difference between the advanced degradation hydrogeomorphology cluster and the non-clustered portions of the site. P-values for the difference in mean value (diamonds) calculated from Welch's *t*-test.

degradation patterns, which may allow for improved predictability and modeling of this process. Therefore, this study emphasizes the need to consider interrelated feedbacks across scales, from the local controls producing meter-scale variability in degradation stage and associated impacts to the regional controls producing this kilometer-scale distribution of degradation.

4.2. Mapping of ice-wedge degradation stages

4.2.1. Detecting and classifying ice-wedge degradation

Local geomorphic complexity is an intrinsic feature of ice-wedge polygon landscapes (Jorgenson et al., 2015; Leffingwell, 1915). Cryogeomorphic processes are responsible for the formation of polygon centers, rims, and troughs with distinct biophysical characteristics over meter-scale ranges. These distinct characteristics are also evolving temporally, first as ice wedges are formed in a sequence of primary, secondary, and tertiary wedges (Haltigin et al., 2012), then as existing ice wedges grow and degrade, developing associated surface expressions related to their geomorphic evolution (Frappier and Lacelle, 2021; Jorgenson et al., 2022; Liljedahl et al., 2016). Multi-scale data proved essential for delineating this local complexity in ice-wedge terrain, though these complex features occasionally hindered identification of degradation stages, given that trough width does not perfectly scale with degradation stage. Distinguishing undegraded, initial degradation, and advanced degradation troughs at the two study sites was a relatively simple task for visual assessment. A handful of troughs at the North Site, however, presented some challenges; it was difficult to distinguish whether these troughs remained in a degraded stage or had progressed to stabilization given the presence of a relict drainage channel and frost boils which interact with the surface pattern of polygons, troughs, and trough vegetation (Fig. S3).

The narrow width of ice-wedge troughs complicates regional mapping of these features even with sub-meter resolution satellite imagery. In particular, the multi-scale approach revealed that satellite detection of troughs systematically undercounts ice wedges in the undegraded and initial degradation stages. Previous work has also exhibited a bias towards mapping ice-wedge troughs in the advanced degradation stage, focusing primarily on flooded thermokarst pits and troughs (Fraser et al., 2018, 2022; Frost et al., 2018; Steedman et al., 2017), due to the ease of detecting surface water in remotely sensed imagery. Mapping of ice-wedge landscapes therefore undercounts the ice wedges that have not yet been fully degraded, but the multi-scale approach also provides a means of accounting for these biases.

Any coarse-resolution mapping of ice-wedge landscapes should incorporate correction factors to account for ice-wedge undercounting. The sensitivity of the satellite detection method in comparison to the drone digitization in this paper could serve as a basis for implementing a correction factor. For example, the satellite trough map accounted for 60% of advanced degradation trough area that was delineated in the drone imagery (Fig. 7). Note, however, that the complexity of ice-wedge landscapes suggests that site-specific corrections will likely be needed. By combining the insights from spaceborne and drone observations, we effectively mitigated biases associated with coarser-scale data, thus enabling a comprehensive analysis of the extent and heterogeneity of ice-wedge degradation.

Degradation stages undergo temporal evolution. While this study offers a snapshot of regional ice-wedge degradation patterns, a thorough evaluation of degradation stages would require a time series analysis of imagery. Previous multi-temporal mapping of ice-wedge degradation highlights the rapid onset of ice-wedge degradation (Farquharson et al., 2019; Jorgenson et al., 2022; Liljedahl et al., 2016) as well as the high spatial variability in degradation patterns (Frost et al., 2018). Time-series mapping, however, is challenging given the limited imagery availability for the Arctic Coastal Plain, and for the Arctic in general. In addition, ice-wedge landscapes are characterized by their seasonal variability in surface water (Koch et al., 2018; Thompson and Woo, 2009), which may affect our ability to identify and accurately classify degradation using remotely sensed imagery. We selected our satellite data to fall within the peak of the summer season (mid-July) to mitigate any seasonal hydrological effects on the classification. Also, while the field data and satellite imagery were collected in differing years (2022 field and drone data, 2014 satellite imagery), all datasets were collected within the same two-week period of July to maintain as much consistency with seasonal hydrology patterns as possible.

The area mapped for this work lacked significant presence of stabilized ice wedges, though the mapping methods provide techniques to

identify stabilization stages in other locations. The hydrogeomorphology clustering method was proposed to identify clusters in four degradation stages based on regional spatial clusters of trough hydrogeomorphology. The advantage of the clustering method is that it highlights the portions of the site with statistically discernible groupings in trough characteristics, allowing for examination of these spatial trends. Analysis focused only on the advanced degradation cluster as the other clusters identified areas with low mapping accuracy (Fig. 11). With a higher-accuracy trough map, this method would be capable of identifying landscape patterns in ice-wedge hydrogeomorphology better. Likewise, the proposed trough width threshold for the thresholding method (Fig. 10) could help distinguish between degraded and stabilized ice wedges given that degraded troughs tend to be narrower, while stabilized troughs tend to be wider (Wickland et al., 2020). Identifying the exact width threshold to distinguish between these categories would likely require site specific data. Furthermore, this threshold-based classification scheme, while simple, does not account for complexities in the landscape such as abnormally wide degraded troughs nor the distinction between primary and secondary troughs. Time-series data would allow examination of the evolution of trough width through time and thus identification of degradation stage with higher confidence.

4.2.2. *Improving permafrost degradation mapping*

Our work represents the first kilometer-scale classification of stages of ice-wedge degradation. Other work that uses remote sensing to identify ice-wedge troughs and degradation stage has relied on manual classification at the local scale (Wickland et al., 2020), which, while effective, is time-consuming and spatially limited. Regional mapping of ice-wedge landscapes has focused on delineating features such as ice-wedge polygons (Abolt et al., 2019; Abolt and Young, 2020; Bhuiyan et al., 2020; Witharana et al., 2020; Zhang et al., 2018, 2020) and troughs (Witharana et al., 2021); our hydrogeomorphology approach extends this delineation work by also classifying the stage of ice-wedge degradation.

The overall accuracy of our satellite-based trough detection method is in line with other optical remote sensing classification methods (e.g., Lara et al., 2018; Raynolds et al., 2019). We presented two complementary accuracy assessment methods for ice-wedge mapping to capture the complexity of mapping and reduce the bias of each individual method. The point-based accuracy assessment has the advantage of covering the entire mapped area, but only captures the accuracy at each individual point. The IoU approach produces a comprehensive spatial analysis of the site of interest but was limited to our two field sites where ground truth data was available. The lower point-based assessment indicates that certain portions of the site are not well-represented by the ice-wedge map, while the higher accuracy of the IoU method indicates that the mapping is performing better in the higher-degradation areas of interest.

The adoption of our proposed hydrogeomorphic approach beyond the kilometer scale to other portions of the Arctic will require careful testing. It is likely that the satellite trough detection method will not accurately identify ice-wedge troughs in all locations, especially those with distinctly different hydrology and vegetation patterns which would impact the NIR and NDVI signals used to identify trough pixels. The hydrogeomorphology-based degradation classification may also require tuning for ice-wedge landscapes with different spectral and geometric characteristics. The combination of multi-scale datasets allowed us to identify the spectral and spatial signatures of ice-wedge degradation stages at this site. We anticipate that incorporating our spectral and geometric classification techniques with a machine learning approach will yield promising results for large-scale mapping and degradation monitoring.

4.3. *Spatial drivers of ice-wedge degradation*

Our study indicates that topography plays a key role influencing kilometer-scale patterns in ice-wedge degradation. The Arctic Coastal Plain gently slopes from the Brooks Range foothills to the Arctic Ocean, with ice-wedge networks spanning the low-stature tundra between thaw lakes (Lara et al., 2018). Elevation fluctuations are evident on the northward sloping terrain, ranging from decimeters to tens of meters (Fig. 9). This varied topography reflects the landscape's history of geomorphic modification through processes such as thaw lake succession (Jones et al., 2022) which influences ground composition, ground ice content, and ice-wedge size. In addition, these topographic patterns influence hydrology regimes and vegetation communities.

We suggest two possible mechanisms associated with topography that may drive the observed clustering of degradation. These factors may be acting independently or in concert with one another (Fig. 14). First, we hypothesize that topography drives unique patterns in soil thermal dynamics. Topography influences soil moisture gradients as higher elevation areas drain towards lower elevation areas (Engstrom et al., 2005). With less moist soils in the higher elevation areas, these portions of the landscape support less productive vegetation and thus less organic (more mineral) soils that offer decreased insulation against thawing (Jafarov and Schaefer, 2016). Conversely, lower elevation areas typically experience higher moisture levels and support greater vegetation productivity, contributing to the soil organic pool and offering enhanced insulation against thawing (Jorgenson et al., 2015). While increased soil moisture increases thermal conductivity, these peat soils offset the increase in conductivity through the absorption of latent heat when pore ice melts (Atchley et al., 2016). Second, we suggest that degradation-topography patterns may be influenced by variations in ground ice content due to differing geomorphic histories. Higher elevation interstitial tundra was likely less impacted by thaw-lake succession, thus would contain older and larger ice wedges that are more susceptible to degradation. Once thawed, these larger ice wedges leave a larger degraded surface. On the other hand, lower elevation areas were more likely impacted by thaw lake succession, where ice wedges may have experienced partial or complete degradation due to the thaw bulb formed under a thaw lake (Grosse et al., 2013; Jones et al., 2022). Consequently, these lower elevation areas may contain more recent and thinner ice wedges, resulting in a less conspicuous degradation signal at the surface.

4.4. *Evolution of heterogeneity through time*

Ice-wedge degradation not only exhibits spatial heterogeneity, but also temporal heterogeneity: degradation may initiate, halt, or advance to stabilization in complex patterns dictated by numerous feedback mechanisms over timescales ranging from hours to centuries (Jorgenson et al., 2015; Kanevskiy et al., 2017). Previous work that examined the spatiotemporal distribution of thermokarst ice-wedge ponds found that pond formation was asynchronous across Arctic Alaska, likely due to regional differences in surface geology, ground ice content, and climate gradients (Frost et al., 2018). Other possible temporal impacts at this site include flooding from the Sagavanirktok River, which has been shown to initiate ice-wedge degradation in flooded polygonal terrain (Zwieback et al., 2023), though this mechanism only impacts the terrain closest to the river and therefore cannot explain the full extent of kilometer-scale patterns identified in this work.

The fate of these ice-wedge systems remains uncertain; it is unknown whether positive feedbacks will intensify thermokarst, ponding, and the formation of thaw lakes (Billings and Peterson, 1980; Jones et al., 2022), or conversely, whether self-limiting feedbacks will halt degradation, drain polygon networks, and move the ice-wedge troughs towards stabilization (Painter et al., 2023). At the meter-scale, ponding and trough widening causes increased degradation (Abolt et al., 2020), yet degradation-induced drainage (Steedman et al., 2017; Webb and Liljedahl, 2023) and increasing biomass (Jorgenson et al., 2015) can halt degradation as well. The spatial patterns in ice wedge age and thus size may also be impacting the observed trends in degradation (Fig. 14).

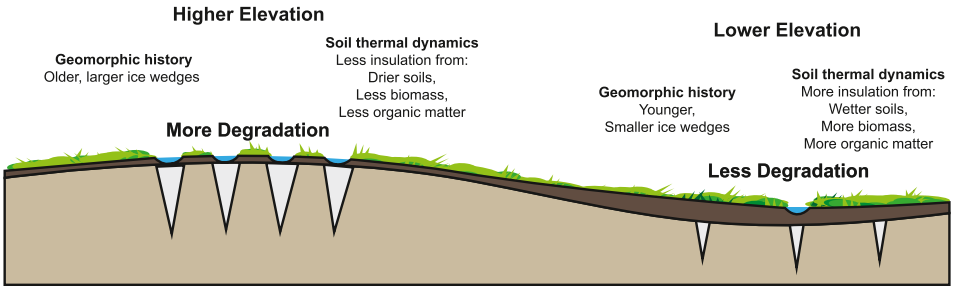

Fig. 14. Conceptual diagram depicting the two proposed mechanisms by which relative elevation, at the kilometer-scale, is driving ice-wedge degradation patterns. First, geomorphic history may cause higher elevation interstitial tundra areas to have older, larger ice wedges that today leave a greater signal of degradation while lower elevation areas tend to have younger, thinner ice wedges. Second, soil thermal dynamics, which are impacted by local hydrology, vegetation, and soil patterns, produce greater insulation above the ice wedges in low elevation portions of the Arctic Coastal Plain. Ice wedges within the low elevation portion of the Plain are therefore more likely to be less degraded, while ice wedges in high elevation portion of the Plain are more susceptible to degradation due to the lesser amount of insulation.

Current field data suggests that ice-wedge degradation remains reversible in Arctic Alaska (Kanevskiy et al., 2022). However, at some point the unprecedented and continuous rise in Arctic temperatures will likely disrupt the stabilization processes by shifting the system to a fundamentally different state. A full understanding of the future evolution of ice-wedge landscapes remains elusive. We need to better understand these spatiotemporal patterns to accurately model the future trajectories of ice-wedge landscapes.

5. Conclusions

Ice-wedge hydrogeomorphology, as proposed in this study, represents a novel technique that allows for mapping ice-wedge degradation stages at broad spatial scales. We characterized and highlighted the spatial heterogeneity in ice-wedge degradation, from the meter to the kilometer scale. In addition, this study yielded new insights into how the spatial variability in ice-wedge degradation is associated with topography patterns both at the meter scale, where degradation occurs in the lowest elevation portions of the trough network, and at the kilometer scale, where clusters of degradation occur in higher topographic positions of the Arctic Coastal Plain.

The high spatial heterogeneity in ice-wedge degradation found in this region demonstrates the need to expand beyond single-site studies and consider disturbance regimes across scales, so that we can improve our understanding of where and why permafrost undergoes thaw and estimate how continued degradation in the Arctic will impact ecosystem function.

The heterogeneity of ice-wedge degradation implies that this system will likely continue to exhibit diverse spatial responses to warming and extreme weather events. However, the ongoing degradation of ice-wedges is likely to drive a regime shift towards a more stable landscape dominated by high-center polygons, with significant structural and functional implications. Understanding the causes and consequences of permafrost degradation heterogeneity offers valuable insights for enhancing its representation in earth system models and unraveling the intricate permafrost-climate feedback of the Arctic system.

CRediT authorship contribution statement

Katherine N. Braun: Writing – review & editing, Writing – original draft, Methodology, Conceptualization. **Christian G. Andresen:** Writing – review & editing, Methodology, Conceptualization.

Declaration of competing interest

The authors declare the following financial interests/personal relationships which may be considered as potential competing interests:

Katherine N Braun reports financial support was provided by NASA. Katherine N Braun reports financial support was provided by National Science Foundation. If there are other authors, they declare that they have no known competing financial interests or personal relationships that could have appeared to influence the work reported in this paper.

Data availability

Data will be made available upon request to the authors.

Acknowledgements

We thank Mark Lara, Caroline Ludden, and Jacob May for help with fieldwork and advice on data analysis and interpretation. Mark Lara and Erika Marín-Spiotta provided helpful comments on the manuscript. This study was supported by NSF ARCSS grant #2311075, NASA FINESST grant #80NSSC24K0037, as well as support to KNB from the Trewartha Research Award, the University of Wisconsin-Madison graduate student fellowship, and by the NSF Graduate Research Fellowship Program under Grant No. DGE-2137424. Any opinions, findings, and conclusions or recommendations expressed in this material are those of the authors and do not necessarily reflect the views of the National Science Foundation. The University Fellowship is provided by the Graduate School, part of the Office of Vice Chancellor for Research and Graduate Education at the University of Wisconsin-Madison, with funding from the Wisconsin Alumni Research Foundation and the UW-Madison. *Geospatial support for this work provided by the Polar Geospatial Center under NSF-OPP awards 1043681, 1559691, and 2129685. ArcticDEM provided by the Polar Geospatial Center under NSF-OPP awards 1043681, 1559691, 1542736, 1810976, and 2129685.*

Appendix A. Supplementary data

Supplementary data to this article can be found online at https://doi.org/10.1016/j.rse.2024.114299.

References

Abolt, C.J., Young, M.H., 2020. High-resolution mapping of spatial heterogeneity in ice wedge polygon geomorphology near Prudhoe Bay, Alaska. Sci. Data 7, 87. https://doi.org/10.1038/s41597-020-0423-9.

Abolt, C.J., Young, M.H., Atchley, A.L., Harp, D.R., 2018. Microtopographic control on the ground thermal regime in ice wedge polygons. Cryosphere 12, 1957–1968. https://doi.org/10.5194/tc-12-1957-2018.

Abolt, C.J., Young, M.H., Atchley, A.L., Wilson, C.J., 2019. Brief communication: rapid machine-learning-based extraction and measurement of ice wedge polygons in high-resolution digital elevation models. Cryosphere 13, 237–245. https://doi.org/10.5194/tc-13-237-2019.

Abolt, C.J., Young, M.H., Atchley, A.L., Harp, D.R., Coon, E.T., 2020. Feedbacks between surface deformation and permafrost degradation in ice wedge polygons, Arctic

coastal plain, Alaska. J. Geophys. Res. Earth 125, e2019JF005349. https://doi.org/10.1029/2019JF005349.
Andresen, C.G., Lawrence, D.M., Wilson, C.J., McGuire, A.D., Koven, C., Schaefer, K., Jafarov, E., Peng, S., Chen, X., Gouttevin, I., Burke, E., Chadburn, S., Ji, D., Chen, G., Hayes, D., Zhang, W., 2020. Soil moisture and hydrology projections of the permafrost region – a model intercomparison. Cryosphere 14, 445–459. https://doi.org/10.5194/tc-14-445-2020.
Anselin, L., 1995. Local indicators of spatial association—LISA. Geogr. Anal. 27, 93–115. https://doi.org/10.1111/j.1538-4632.1995.tb00338.x.
Atchley, A.L., Coon, E.T., Painter, S.L., Harp, D.R., Wilson, C.J., 2016. Influences and interactions of inundation, peat, and snow on active layer thickness. Geophys. Res. Lett. 43, 5116–5123. https://doi.org/10.1002/2016GL068550.
Bailey, R.G., 1995. Arctic Tundra Province [WWW Document]. Description of the Ecoregions of the United States. URL. https://www.fs.fed.us/land/ecosysmgmt/colorimagemap/images/124.html (accessed 11.12.21).
Bhuiyan, M.A.E., Witharana, C., Liljedahl, A.K., 2020. Use of very high spatial resolution commercial satellite imagery and deep learning to automatically map ice-wedge polygons across tundra vegetation types. J. Imaging 6, 137. https://doi.org/10.3390/jimaging6120137.
Billings, W.D., Peterson, K.M., 1980. Vegetational change and ice-wedge polygons through the thaw-lake cycle in Arctic Alaska. Arct. Alp. Res. 12, 413–432. https://doi.org/10.1080/00040851.1980.12004204.
Black, R.F., 1982. Ice-wedge polygons of northern Alaska. In: Coates, D.R. (Ed.), Glacial Geomorphology. Springer Netherlands, Dordrecht, pp. 247–275. https://doi.org/10.1007/978-94-011-6491-7_9.
Chen, J., Wang, G., Luo, L., Gong, W., Cheng, Z., 2021. Building area estimation in drone aerial images based on mask R-CNN. IEEE Geosci. Remote Sens. Lett. 18, 891–894. https://doi.org/10.1109/LGRS.2020.2988326.
Connon, R., Devoie, É., Hayashi, M., Veness, T., Quinton, W., 2018. The influence of shallow taliks on permafrost thaw and active layer dynamics in subarctic Canada. J. Geophys. Res. Earth 123, 281–297. https://doi.org/10.1002/2017JF004469.
Cryosol Working Group, 2014. Northern and Mid-Latitude Soil Database. https://doi.org/10.3334/ORNLDAAC/705.
de Mendiburu, F., Yaseen, M., 2020. Agricolae: Statistical Procedures for Agricultural Research.
Engstrom, R., Hope, A., Kwon, H., Stow, D., Zamolodchikov, D., 2005. Spatial distribution of near surface soil moisture and its relationship to microtopography in the Alaskan Arctic coastal plain. Hydrol. Res. 36, 219–234. https://doi.org/10.2166/nh.2005.0016.
Farquharson, L.M., Romanovsky, V.E., Cable, W.L., Walker, D.A., Kokelj, S.V., Nicolsky, D., 2019. Climate change drives widespread and rapid Thermokarst development in very cold permafrost in the Canadian high Arctic. Geophys. Res. Lett. 46, 6681–6689. https://doi.org/10.1029/2019GL082187.
Feuillet, T., Birre, D., Milian, J., Godard, V., Clauzel, C., Serrano-Notivoli, R., 2020. Spatial dynamics of alpine tree lines under global warming: what explains the mismatch between tree densification and elevational upward shifts at the tree line ecotone? J. Biogeogr. 47, 1056–1068. https://doi.org/10.1111/jbi.13779.
Forte, E., French, H.M., Raffi, R., Santin, I., Guglielmin, M., 2022. Investigations of polygonal patterned ground in continuous Antarctic permafrost by means of ground penetrating radar and electrical resistivity tomography: some unexpected correlations. Permafr. Periglac. Process. 33, 1–15. https://doi.org/10.1002/ppp.2156.
Frappier, R., Lacelle, D., 2021. Distribution, morphometry, and ice content of ice-wedge polygons in Tombstone Territorial Park, Central Yukon, Canada. Permafr. Periglac. Process. 32, 587–600. https://doi.org/10.1002/ppp.2123.
Fraser, R.H., Kokelj, S.V., Lantz, T.C., McFarlane-Winchester, M., Olthof, I., Lacelle, D., 2018. Climate sensitivity of high Arctic permafrost terrain demonstrated by widespread ice-wedge thermokarst on Banks Island. Remote Sens. 10, 954. https://doi.org/10.3390/rs10060954.
Fraser, R.H., McFarlane-Winchester, M., Kokelj, S.V., 2022. Recent ponding of upland ice-wedge polygon networks detected across the Canadian Arctic archipelago using satellite remote sensing (no. 69). Geomat. Canada. https://doi.org/10.4095/329618.
French, H.M., 2017. The Periglacial Environment. John Wiley & Sons.
Frost, G.V., Christopherson, T., Jorgenson, M.T., Liljedahl, A.K., Macander, M.J., Walker, D.A., Wells, A.F., 2018. Regional patterns and asynchronous onset of ice-wedge degradation since the mid-20th century in Arctic Alaska. Remote Sens. 10, 1312. https://doi.org/10.3390/rs10081312.
Garrigues, S., Allard, D., Baret, F., Weiss, M., 2006. Quantifying spatial heterogeneity at the landscape scale using variogram models. Remote Sens. Environ. 103, 81–96. https://doi.org/10.1016/j.rse.2006.03.013.
Grosse, G., Jones, B., Arp, C., 2013. Thermokarst Lakes, drainage, and drained basins. In: Shroder, J.F. (Ed.), Treatise on Geomorphology. Academic Press, San Diego, pp. 325–353. https://doi.org/10.1016/B978-0-12-374739-6.00216-5.
Haltigin, T.W., Pollard, W.H., Dutilleul, P., Osinski, G.R., 2012. Geometric evolution of polygonal terrain networks in the Canadian high Arctic: evidence of increasing regularity over time. Permafr. Periglac. Process. 23, 178–186. https://doi.org/10.1002/ppp.1741.
Haralick, R.M., Sternberg, S.R., Zhuang, X., 1987. Image analysis using mathematical morphology. IEEE Trans. Pattern Anal. Mach. Intell. PAMI-9, 532–550. https://doi.org/10.1109/TPAMI.1987.4767941.
Henn, J.J., Anderson, C.B., Martínez Pastur, G., 2016. Landscape-level impact and habitat factors associated with invasive beaver distribution in Tierra del Fuego. Biol. Invasions 18, 1679–1688. https://doi.org/10.1007/s10530-016-1110-9.
Hinkel, K.M., Eisner, W.R., Bockheim, J.G., Nelson, F.E., Peterson, K.M., Dai, X., 2003. Spatial extent, age, and carbon stocks in drained thaw lake basins on the Barrow peninsula, Alaska. Arct. Antarct. Alp. Res. 35, 291–300. https://doi.org/10.1657/1523-0430(2003)035[0291:SEAACS]2.0.CO;2.
Homer, C., Dewitz, J., Yang, L., Jin, S., Danielson, P., Xian, G., Coulston, J., Herold, N., Wickham, J., Megown, K., 2015. Completion of the 2011 National Land Cover Database for the conterminous United States – representing a decade of land cover change information. Photogramm. Eng. Remote. Sens. 81, 345–354.
Hsu, A.J., Kumagai, J., Favoretto, F., Dorian, J., Guerrero Martinez, B., Aburto-Oropeza, O., 2020. Driven by drones: improving mangrove extent maps using high-resolution remote sensing. Remote Sens. 12, 3986. https://doi.org/10.3390/rs12233986.
Jafarov, E., Schaefer, K., 2016. The importance of a surface organic layer in simulating permafrost thermal and carbon dynamics. Cryosphere 10, 465–475. https://doi.org/10.5194/tc-10-465-2016.
Jones, A., Stolbovoy, V., Tarnocai, C., Broll, G., Spaargaren, O., Montanarella, L., 2008. Soil Atlas of the Northern Circumpolar Region. European Commission, Publications Office of the European Union, Luxembourg.
Jones, B.M., Grosse, G., Farquharson, L.M., Roy-Léveillée, P., Veremeeva, A., Kanevskiy, M.Z., Gaglioti, B.V., Breen, A.L., Parsekian, A.D., Ulrich, M., Hinkel, K. M., 2022. Lake and drained lake basin systems in lowland permafrost regions. Nat. Rev. Earth Environ. 3, 85–98. https://doi.org/10.1038/s43017-021-00238-9.
Jorgenson, M.T., Shur, Y.L., Pullman, E.R., 2006. Abrupt increase in permafrost degradation in Arctic Alaska. Geophys. Res. Lett. 33 https://doi.org/10.1029/2005GL024960.
Jorgenson, M.T., Kanevskiy, M., Shur, Y., Moskalenko, N., Brown, D.R.N., Wickland, K., Striegl, R., Koch, J., 2015. Role of ground ice dynamics and ecological feedbacks in recent ice wedge degradation and stabilization. J. Geophys. Res. Earth 120, 2280–2297. https://doi.org/10.1002/2015JF003602.
Jorgenson, M.T., Kanevskiy, M.Z., Jorgenson, J.C., Liljedahl, A., Shur, Y., Epstein, H., Kent, K., Griffin, C.G., Daanen, R., Boldenow, M., Orndahl, K., Witharana, C., Jones, B.M., 2022. Rapid transformation of tundra ecosystems from ice-wedge degradation. Glob. Planet. Chang. 216, 103921 https://doi.org/10.1016/j.gloplacha.2022.103921.
Kalacska, M., Lucanus, O., Arroyo-Mora, J.P., Laliberté, É., Elmer, K., Leblanc, G., Groves, A., 2020. Accuracy of 3D landscape reconstruction without ground control points using different UAS platforms. Drones 4. https://doi.org/10.3390/drones4020013.
Kanevskiy, M., Shur, Y., Jorgenson, M.T., Ping, C.-L., Michaelson, G.J., Fortier, D., Stephani, E., Dillon, M., Tumskoy, V., 2013. Ground ice in the upper permafrost of the Beaufort Sea coast of Alaska. Cold Reg. Sci. Technol. 85, 56–70. https://doi.org/10.1016/j.coldregions.2012.08.002.
Kanevskiy, M., Shur, Y., Jorgenson, T., Brown, D.R.N., Moskalenko, N., Brown, J., Walker, D.A., Raynolds, M.K., Buchhorn, M., 2017. Degradation and stabilization of ice wedges: implications for assessing risk of thermokarst in northern Alaska. Geomorphology 297, 20–42. https://doi.org/10.1016/j.geomorph.2017.09.001.
Kanevskiy, Mikhail, Shur, Y., Walker, S., Jorgenson, T., Raynolds, M., Peirce, J., Jones, B., Buchhorn, M., Matyshak, G., Bergstedt, H., Breen, A., Connor, B., Daanen, Ronald, Liljedahl, A., Romanovsky, V., Kanevskiy, M., Shur, Y., Daanen, R., 2022. The Shifting Mosaic of Ice-Wedge Degradation and Stabilization in Response to Infrastructure and Climate Change. Prudhoe Bay Oilfield, Alaska, USA (Arctic Science 1–33).
Kassambara, A., 2023. ggpubr: "ggplot2". Based Publication Ready Plots.
Koch, J.C., Jorgenson, M.T., Wickland, K.P., Kanevskiy, M., Striegl, R., 2018. Ice wedge degradation and stabilization impact water budgets and nutrient cycling in Arctic trough ponds. J. Geophys. Res. Biogeosci. 123, 2604–2616. https://doi.org/10.1029/2018JG004528.
Lachenbruch, A.H., 1962. Mechanics of Thermal Contraction Cracks and Ice-Wedge Polygons in Permafrost. Geological Society of America.
Lara, M.J., McGuire, A.D., Euskirchen, E.S., Tweedie, C.E., Hinkel, K.M., Skurikhin, A.N., Romanovsky, V.E., Grosse, G., Bolton, W.R., Genet, H., 2015. Polygonal tundra geomorphological change in response to warming alters future CO2 and CH4 flux on the Barrow peninsula. Glob. Chang. Biol. 21, 1634–1651. https://doi.org/10.1111/gcb.12757.
Lara, M.J., Nitze, I., Grosse, G., McGuire, A.D., 2018. Tundra landform and vegetation productivity trend maps for the Arctic coastal plain of northern Alaska. Sci. Data 5, 180058. https://doi.org/10.1038/sdata.2018.58.
Leffingwell, E.D.K., 1915. Ground-ice wedges: the dominant form of ground-ice on the north coast of Alaska. J. Geol. 23, 635–654. https://doi.org/10.1086/622281.
Liljedahl, A.K., Boike, J., Daanen, R.P., Fedorov, A.N., Frost, G.V., Grosse, G., Hinzman, L.D., Iijma, Y., Jorgenson, J.C., Matveyeva, N., Necsoiu, M., Raynolds, M. K., Romanovsky, V.E., Schulla, J., Tape, K.D., Walker, D.A., Wilson, C.J., Yabuki, H., Zona, D., 2016. Pan-Arctic ice-wedge degradation in warming permafrost and its influence on tundra hydrology. Nat. Geosci. 9, 312–318. https://doi.org/10.1038/ngeo2674.
Liu, L., Zhang, T., Wahr, J., 2010. InSAR measurements of surface deformation over permafrost on the north slope of Alaska. J. Geophys. Res. Earth 115. https://doi.org/10.1029/2009JF001547.
Loke, L.H.L., Chisholm, R.A., 2022. Measuring habitat complexity and spatial heterogeneity in ecology. Ecol. Lett. 25, 2269–2288. https://doi.org/10.1111/ele.14084.
Macander, M.J., Frost, G.V., Nelson, P.R., Swingley, C.S., 2017. Regional quantitative cover mapping of tundra plant functional types in Arctic Alaska. Remote Sens. 9, 1024. https://doi.org/10.3390/rs9101024.
Mackay, J.R., 1993. Air temperature, snow cover, creep of frozen ground, and the time of ice-wedge cracking, western Arctic coast. Can. J. Earth Sci. 30, 1720–1729. https://doi.org/10.1139/e93-151.

Marcot, B.G., Jorgenson, M.T., Lawler, J.P., Handel, C.M., DeGange, A.R., 2015. Projected changes in wildlife habitats in Arctic natural areas of Northwest Alaska. Clim. Chang. 130, 145–154. https://doi.org/10.1007/s10584-015-1354-x.

Martin, A.F., Lantz, T.C., Humphreys, E.R., 2018. Ice wedge degradation and CO2 and CH4 emissions in the Tuktoyaktuk coastlands, Northwest Territories. Arctic Sci. 4, 130–145. https://doi.org/10.1139/as-2016-0011.

Maurer, T., 2013. How to pan-sharpen images using the gram-Schmidt pan-sharpen method - a recipe. In: The International Archives of the Photogrammetry, Remote Sensing and Spatial Information Sciences XL-1-W1, pp. 239–244. https://doi.org/10.5194/isprsarchives-XL-1-W1-239-2013.

Murakami, A., Medrial Zain, A., Takeuchi, K., Tsunekawa, A., Yokota, S., 2005. Trends in urbanization and patterns of land use in the Asian mega cities Jakarta, Bangkok, and metro Manila. In: Landscape and Urban Planning, Ecological Dynamics of Urban and Rural Landscapes in East Asia, 70, pp. 251–259. https://doi.org/10.1016/j.landurbplan.2003.10.021.

Necsoiu, M., Dinwiddie, C.L., Walter, G.R., Larsen, A., Stothoff, S.A., 2013. Multi-temporal image analysis of historical aerial photographs and recent satellite imagery reveals evolution of water body surface area and polygonal terrain morphology in Kobuk Valley National Park, Alaska. Environ. Res. Lett. 8, 025007 https://doi.org/10.1088/1748-9326/8/2/025007.

Nitzbon, J., Langer, M., Martin, L.C.P., Westermann, S., Schneider von Deimling, T., Boike, J., 2021. Effects of multi-scale heterogeneity on the simulated evolution of ice-rich permafrost lowlands under a warming climate. Cryosphere 15, 1399–1422. https://doi.org/10.5194/tc-15-1399-2021.

Ogle, D.H., Doll, J.C., Wheeler, A.P., Dinno, A., 2023. FSA: Simple Fisheries Stock Assessment Methods.

Opel, T., Meyer, H., Wetterich, S., Laepple, T., Dereviagin, A., Murton, J., 2018. Ice wedges as archives of winter paleoclimate: a review. Permafr. Periglac. Process. 29, 199–209. https://doi.org/10.1002/ppp.1980.

Oyana, T.J., 2020. Spatial Analysis with R: Statistics, Visualization, and Computational Methods. CRC Press.

Painter, S.L., Coon, E.T., Khattak, A.J., Jastrow, J.D., 2023. Drying of tundra landscapes will limit subsidence-induced acceleration of permafrost thaw. Proc. Natl. Acad. Sci. USA 120, e2212171120. https://doi.org/10.1073/pnas.2212171120.

Parkinson, R.J., 1978. Genesis and Classification of Arctic Coastal Plain Soils, Prudhoe Bay, Alaska (No. 68). Institute of Polar Studies.

Pedersen, T.L., 2024. Patchwork: The Composer of Plots.

Pickett, S.T.A., Cadenasso, M.L., 1995. Landscape ecology: spatial heterogeneity in ecological systems. Science 269, 331–334.

Plug, L.J., Werner, B.T., 2002. Nonlinear dynamics of ice-wedge networks and resulting sensitivity to severe cooling events. Nature 417, 929–933. https://doi.org/10.1038/nature00796.

Porter, C., Morin, P., Howat, I., Noh, M.-J., Bates, B., Peterman, K., Keesey, S., Schlenk, M., Gardiner, J., Tomko, K., Willis, M., Kelleher, C., Cloutier, M., Husby, E., Foga, S., Nakamura, H., Platson, M., Wethington, M., Williamson, C., Bauer, G., Enos, J., Arnold, G., Kramer, W., Becker, P., Doshi, A., D'Souza, C., Cummens, P., Laurier, F., Bojesen, M., 2022. ArcticDEM. Version 3. https://doi.org/10.7910/DVN/OHHUKH.

Rawlinson, S., 1990. Surficial Geology and Morphology of the Alaskan Central Arctic Coastal Plain. University of Alaska Fairbanks, Fairbanks, Alaska.

Raynolds, M.K., Walker, D.A., Balser, A., Bay, C., Campbell, M., Cherosov, M.M., Daniëls, F.J.A., Eidesen, P.B., Ermokhina, K.A., Frost, G.V., Jedrzejek, B., Jorgenson, M.T., Kennedy, B.E., Kholod, S.S., Lavrinenko, I.A., Lavrinenko, O.V., Magnússon, B., Matveyeva, N.V., Metúsalemsson, S., Nilsen, L., Olthof, I., Pospelov, I.N., Pospelova, E.B., Pouliot, D., Razzhivin, V., Schaepman-Strub, G., Šibík, J., Telyatnikov, M.Yu., Troeva, E., 2019. A raster version of the circumpolar Arctic vegetation map (CAVM). Remote Sens. Environ. 232, 111297 https://doi.org/10.1016/j.rse.2019.111297.

Rettelbach, T., Langer, M., Nitze, I., Jones, B., Helm, V., Freytag, J.-C., Grosse, G., 2021. A quantitative graph-based approach to monitoring ice-wedge trough dynamics in polygonal permafrost landscapes. Remote Sens. 13, 3098. https://doi.org/10.3390/rs13163098.

Rezatofighi, H., Tsoi, N., Gwak, J., Sadeghian, A., Reid, I., Savarese, S., 2019. Generalized intersection over union: A metric and a loss for bounding box regression. In: 2019 IEEE/CVF Conference on Computer Vision and Pattern Recognition (CVPR). Presented at the 2019 IEEE/CVF Conference on Computer Vision and Pattern Recognition (CVPR). IEEE, Long Beach, CA, USA, pp. 658–666. https://doi.org/10.1109/CVPR.2019.00075.

Sarkar, D., 2008. Lattice: Multivariate Data Visualization with R. Springer, New York.

Schuur, E.A.G., McGuire, A.D., Schädel, C., Grosse, G., Harden, J.W., Hayes, D.J., Hugelius, G., Koven, C.D., Kuhry, P., Lawrence, D.M., Natali, S.M., Olefeldt, D., Romanovsky, V.E., Schaefer, K., Turetsky, M.R., Treat, C.C., Vonk, J.E., 2015. Climate change and the permafrost carbon feedback. Nature 520, 171–179. https://doi.org/10.1038/nature14338.

Siewert, M.B., Lantuit, H., Richter, A., Hugelius, G., 2021. Permafrost causes unique fine-scale spatial variability across tundra soils. Glob. Biogeochem. Cycles 35. https://doi.org/10.1029/2020GB006659.

Steedman, A.E., Lantz, T.C., Kokelj, S.V., 2017. Spatio-temporal variation in high-Centre polygons and ice-wedge melt ponds, Tuktoyaktuk coastlands, Northwest Territories. Permafr. Periglac. Process. 28, 66–78. https://doi.org/10.1002/ppp.1880.

Thompson, D.K., Woo, M.-K., 2009. Seasonal hydrochemistry of a high Arctic wetland complex. Hydrol. Process. 23, 1397–1407. https://doi.org/10.1002/hyp.7271.

Turetsky, M.R., Abbott, B.W., Jones, M.C., Anthony, K.W., Olefeldt, D., Schuur, E.A.G., Grosse, G., Kuhry, P., Hugelius, G., Koven, C., Lawrence, D.M., Gibson, C., Sannel, A. B.K., McGuire, A.D., 2020. Carbon release through abrupt permafrost thaw. Nat. Geosci. 13, 138–143. https://doi.org/10.1038/s41561-019-0526-0.

Vincent, W.F., Lemay, M., Allard, M., 2017. Arctic permafrost landscapes in transition: towards an integrated earth system approach. Arctic Sci. 3, 39–64. https://doi.org/10.1139/as-2016-0027.

Wainwright, H.M., Dafflon, B., Smith, L.J., Hahn, M.S., Curtis, J.B., Wu, Y., Ulrich, C., Peterson, J.E., Torn, M.S., Hubbard, S.S., 2015. Identifying multiscale zonation and assessing the relative importance of polygon geomorphology on carbon fluxes in an Arctic tundra ecosystem. J. Geophys. Res. Biogeosci. 120, 788–808. https://doi.org/10.1002/2014JG002799.

Wainwright, H.M., Oktem, R., Dafflon, B., Dengel, S., Curtis, J.B., Torn, M.S., Cherry, J., Hubbard, S.S., 2021. High-resolution spatio-temporal estimation of net ecosystem exchange in ice-wedge polygon tundra using in situ sensors and remote sensing data. Land 10, 722. https://doi.org/10.3390/land10070722.

Walker, D.A., Raynolds, M.K., Kanevskiy, M.Z., Shur, Y.S., Romanovsky, V.E., Jones, B. M., Buchhorn, M., Jorgenson, M.T., Šibík, J., Breen, A.L., Kade, A., Watson-Cook, E., Bergstedt, H., Liljedahl, A.K., Daanen, R.P., Connor, B., Nicolsky, D., Peirce, J.L., 2022. Cumulative Impacts of a Gravel Road and Climate Change in an Ice-Wedge Polygon Landscape, Prudhoe Bay, AK. Arctic Science. https://doi.org/10.1139/AS-2021-0014.

Webb, E.E., Liljedahl, A.K., 2023. Diminishing lake area across the northern permafrost zone. Nat. Geosci. 1–8 https://doi.org/10.1038/s41561-023-01128-z.

Weiss, A., 2001. Topographic position and landforms analysis. In: Presented at the ESRI User Conference, San Diego, CA.

Westoby, M.J., Brasington, J., Glasser, N.F., Hambrey, M.J., Reynolds, J.M., 2012. 'Structure-from-motion' photogrammetry: a low-cost, effective tool for geoscience applications. Geomorphology 179, 300–314. https://doi.org/10.1016/j.geomorph.2012.08.021.

Wickham, H., 2016. ggplot2: Elegant Graphics for Data Analysis. Springer-Verlag, New York.

Wickham, H., Averick, M., Bryan, J., Chang, W., McGowan, L.D., François, R., Grolemund, G., Hayes, A., Henry, L., Hester, J., Kuhn, M., Pedersen, T.L., Miller, E., Bache, S.M., Müller, K., Ooms, J., Robinson, D., Seidel, D.P., Spinu, V., Takahashi, K., Vaughan, D., Wilke, C., Woo, K., Yutani, H., 2019. Welcome to the tidyverse. J. Open Source Softw. 4, 1686. https://doi.org/10.21105/joss.01686.

Wickham, H., François, R., Henry, L., Müller, K., Vaughan, D., 2023. Dplyr: A Grammar of Data Manipulation.

Wickland, K.P., Jorgenson, M.T., Koch, J.C., Kanevskiy, M., Striegl, R., 2020. Carbon dioxide and methane flux in a dynamic Arctic tundra landscape: decadal-scale impacts of ice wedge degradation and stabilization. Geophys. Res. Lett. 47.

Witharana, C., Bhuiyan, M.A.E., Liljedahl, A.K., Kanevskiy, M., Epstein, H.E., Jones, B. M., Daanen, R., Griffin, C.G., Kent, K., Ward Jones, M.K., 2020. Understanding the synergies of deep learning and data fusion of multispectral and panchromatic high resolution commercial satellite imagery for automated ice-wedge polygon detection. ISPRS J. Photogramm. Remote Sens. 170, 174–191. https://doi.org/10.1016/j.isprsjprs.2020.10.010.

Witharana, C., Bhuiyan, M.A.E., Liljedahl, A.K., Kanevskiy, M., Jorgenson, T., Jones, B. M., Daanen, R., Epstein, H.E., Griffin, C.G., Kent, K., Ward Jones, M.K., 2021. An object-based approach for mapping tundra ice-wedge polygon troughs from very high spatial resolution optical satellite imagery. Remote Sens. 13, 558. https://doi.org/10.3390/rs13040558.

Wolter, J., Lantuit, H., Fritz, M., Macias-Fauria, M., Myers-Smith, I., Herzschuh, U., 2016. Vegetation composition and shrub extent on the Yukon coast, Canada, are strongly linked to ice-wedge polygon degradation. Polar Res. 35, 27489. https://doi.org/10.3402/polar.v35.27489.

Zhang, W., Witharana, C., Liljedahl, A.K., Kanevskiy, M., 2018. Deep convolutional neural networks for automated characterization of Arctic ice-wedge polygons in very high spatial resolution aerial imagery. Remote Sens. 10, 1487. https://doi.org/10.3390/rs10091487.

Zhang, W., Liljedahl, A.K., Kanevskiy, M., Epstein, H.E., Jones, B.M., Jorgenson, M.T., Kent, K., 2020. Transferability of the deep learning mask R-CNN model for automated mapping of ice-wedge polygons in high-resolution satellite and UAV images. Remote Sens. 12, 1085. https://doi.org/10.3390/rs12071085.

Zwieback, S., McClernan, M., Kanevskiy, M., Jorgenson, M.T., Walker, D.A., Chang, Q., Bergstedt, H., Toniolo, H., Romanovsky, V.E., Meyer, F.J., 2023. Disparate permafrost terrain changes after a large flood observed from space. Permafr. Periglac. Process. 34, 451–466. https://doi.org/10.1002/ppp.2208.